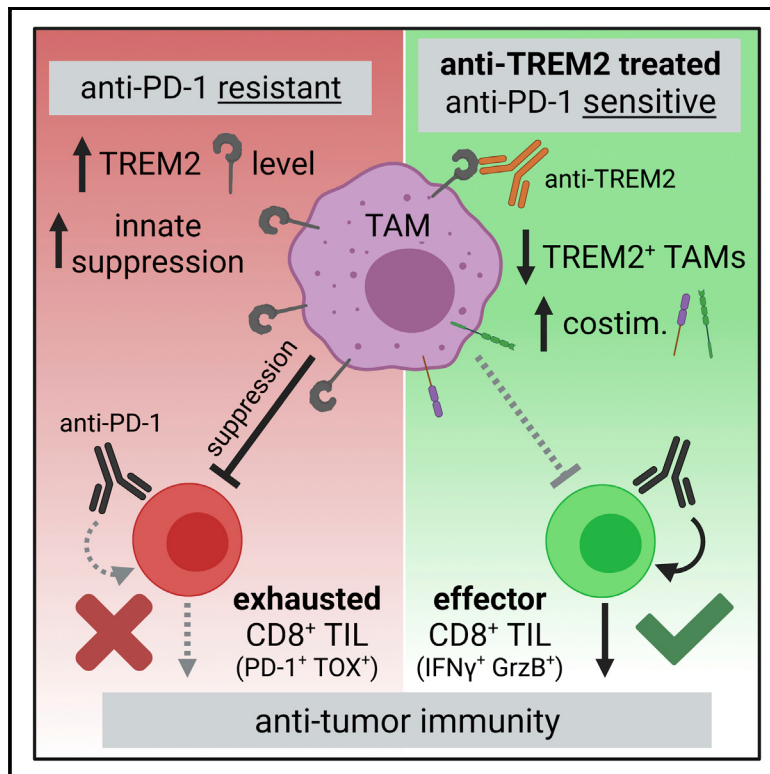


## Targeting TREM2 on tumor-associated macrophages enhances immunotherapy

### Graphical abstract



### Authors

Mikhail Binnewies, Joshua L. Pollack,  
Joshua Rudolph, ..., Matthew F. Krummel,  
Michel Streuli, Venkataraman Sriram

### Correspondence

kbaker@pionyrtx.com (K.P.B.),  
matthew.krummel@ucsf.edu (M.F.K.),  
vesriram@gmail.com (V.S.)

### In brief

Binnewies et al. show that TREM2-expressing tumor-associated macrophages (TAMs) are critical mediators of immune suppression in the tumor microenvironment (TME) and correlate with T cell exhaustion in human cancer. Effector-enhanced anti-TREM2 antibody treatment alters the abundance and phenotype of TAMs in the TME and sensitizes the response to anti-PD-1 therapy.

### Highlights

- TAM-expressed TREM2 is associated with T cell exhaustion and anti-PD-1 resistance
- Effector-enhanced anti-TREM2 antibody treatment drives anti-tumor immunity
- TAM abundance and suppression are reduced following anti-TREM2 therapy
- Anti-TREM2 therapy potentiates T cell activation and response to anti-PD-1 treatment



## Article

# Targeting TREM2 on tumor-associated macrophages enhances immunotherapy

Mikhail Binnewies,<sup>1</sup> Joshua L. Pollack,<sup>1</sup> Joshua Rudolph,<sup>1</sup> Subhadra Dash,<sup>1</sup> Marwan Abushawish,<sup>1</sup> Tian Lee,<sup>1</sup> Nadine S. Jahchan,<sup>1</sup> Pamela Canaday,<sup>1</sup> Erick Lu,<sup>1</sup> Manith Norng,<sup>1</sup> Shilpa Mankikar,<sup>1</sup> Victoria M. Liu,<sup>1</sup> Xiaoyan Du,<sup>1</sup> Amanda Chen,<sup>1</sup> Ranna Mehta,<sup>1</sup> Rachael Palmer,<sup>1</sup> Vladislava Juric,<sup>1</sup> Linda Liang,<sup>1</sup> Kevin P. Baker,<sup>1,3,\*</sup> Leonard Reyno,<sup>1</sup> Matthew F. Krummel,<sup>2,\*</sup> Michel Streuli,<sup>1</sup> and Venkataraman Sriram<sup>1,\*</sup>

<sup>1</sup>Pionyr Immunotherapeutics, South San Francisco, CA 94080, USA

<sup>2</sup>Department of Pathology, University of California, San Francisco, San Francisco, CA 94143, USA

<sup>3</sup>Lead contact

\*Correspondence: kbaker@pionyrtx.com (K.P.B.), matthew.krummel@ucsf.edu (M.F.K.), vesriram@gmail.com (V.S.)

<https://doi.org/10.1016/j.celrep.2021.109844>

## SUMMARY

Converting checkpoint inhibitor (CPI)-resistant individuals to being responsive requires identifying suppressive mechanisms. We identify TREM2<sup>+</sup> tumor-associated macrophages (TAMs) as being correlated with exhausted CD8<sup>+</sup> tumor-infiltrating lymphocytes (TILs) in mouse syngeneic tumor models and human solid tumors of multiple histological types. Fc domain-enhanced anti-TREM2 monoclonal antibody (mAb) therapy promotes anti-tumor immunity by elimination and modulation of TAM populations, which leads to enhanced CD8<sup>+</sup> TIL infiltration and effector function. TREM2<sup>+</sup> TAMs are most enriched in individuals with ovarian cancer, where TREM2 expression corresponds to disease grade accompanied by worse recurrence-free survival. In an aggressive orthotopic ovarian cancer model, anti-TREM2 mAb therapy drives potent anti-tumor immunity. These results highlight TREM2 as a highly attractive target for immunotherapy modulation in individuals who are refractory to CPI therapy and likely have a TAM-rich tumor microenvironment.

## INTRODUCTION

Checkpoint inhibitor (CPI) therapies elicit durable responses across a broad range of cancer indications, including metastatic melanoma, non-small cell lung cancer (NSCLC), and renal cancer (Wilky, 2019). However, only a subset of individuals within each of these indications responds to treatment (Jenkins et al., 2018). The basis for CPI failure involves multiple mechanisms, including lack of tumor neoantigens (Jenkins et al., 2018; Le et al., 2017), failure to reverse T cell exhaustion (Miller et al., 2019; Pauken et al., 2016; Philip et al., 2017), and intra-tumoral presence of immunosuppressive immune cells, including tumor-associated macrophages (TAMs) (Dammeijer et al., 2017; Dannenmann et al., 2013; Jahchan et al., 2019). TAMs are believed to promote CPI resistance through mechanisms that subvert anti-tumor immunity (DeNardo and Ruffell, 2019) and promote tumor growth (Lewis and Pollard, 2006). TAMs can directly (Peranzoni et al., 2018; Viitala et al., 2019; Wang et al., 2015) and indirectly suppress CD8<sup>+</sup> tumor-infiltrating lymphocyte (TIL) function, drive immunosuppression through secretion of factors like interleukin-10 (IL-10) (Ruffell et al., 2014), and promote tumor cell proliferation and extravasation by supporting vascularization and development of extracellular matrices (ECMs) (Lin and Pollard, 2007; Penny et al., 2016; Qian et al., 2009). Clinically, high frequencies of intratumoral TAMs correlate with poor prognosis across multiple solid tumor indications (Komohara et al., 2014; Zhang et al., 2012), signifying their role as

central mediators of immune suppression in the tumor microenvironment (TME). Consequently, reducing TAM frequency and/or modulating TAM function is a promising strategy to convert CPI-resistant individuals into CPI-sensitive individuals.

Therapeutic targeting of TAMs and related immunosuppressive myeloid cells has so far had a minimal effect on improving clinical outcomes (Butowski et al., 2016; Calvo et al., 2017; Jahchan et al., 2019; Nywening et al., 2016). For instance, therapies that reduce the global abundance of macrophages are associated with paltry anti-tumor responses, likely because of poor tumor specificity (Jahchan et al., 2019). It is also likely that, although some TAMs are highly immunosuppressive, others are essential for tumor clearance.

Consequently, new approaches are needed to more precisely target TAMs as well as other immunosuppressive, tumor-associated myeloid cell populations (Broz et al., 2014) to improve the efficacy and safety associated with myeloid cell-targeting therapies.

Here we report transmembrane protein triggering receptor expressed on myeloid cells 2 (TREM2) as a highly promising therapeutic target because of its enriched expression on TAMs and known immunosuppressive function in human and mouse. TREM2 has been studied widely in microglia, where TREM2 functions in neuronal debris clearance to counteract the inflammatory response (Takahashi et al., 2005). Based on the known functions of TREM2 in microglial pathophysiology and recent work on TAMs in the TME, it is postulated that TREM2 on



TAMs dampens inflammatory gene expression directly through its association with DNAX-activating protein of 12 kDa (DAP12) and indirectly through promotion of apoptotic cell clearance. In the present study, we found that TREM2<sup>+</sup> TAMs corresponded to a highly immunosuppressed TME in mouse and human. Treatment of tumor-bearing animals with an Fc domain-enhanced anti-TREM2 monoclonal antibody (mAb) led to depletion of TAMs and drove anti-tumor immunity as a single agent and when combined with anti-PD-1. Further, we identified ovarian cancer as an ideal tumor indication for anti-TREM2 mAb therapy because of its poor response to CPI, high expression of TREM2, and high density of TAMs and based on the anti-tumor response to anti-TREM2 mAb in a preclinical orthotopic model of ovarian cancer. Our work not only confirms the recent findings of others but extends into a highly translationally focused, clinically relevant assessment of TREM2 on TAMs. Furthermore, we enabled not only our own findings but the findings of others by developing an anti-TREM2 mAb clinical asset that is currently being tested in humans (ClinicalTrials.gov: NCT04691375).

## RESULTS

### TREM2 expression is correlated with immune exhaustion and anti-PD-1 resistance in the mouse

To identify genes that are significantly upregulated by TAMs in human tumor indications with a low response rate to anti-PD-1 treatment (Matulonis et al., 2019), we sorted CD45<sup>+</sup> immune cells from a dissociated human ovarian tumor and then performed single-cell RNA sequencing (scRNA-seq). After removing dead cells from analysis, processing of 8,954 cells using Seurat (Stuart et al., 2019) led to 16 unique transcriptional clusters of myeloid and lymphoid origin (Figures 1A and 1B). Differential expression (DE) analysis between all populations identified in Figure 1A revealed genes that are enriched specifically within TAMs and identified the cell surface molecule TREM2 as being highly expressed in TAMs compared with other immune populations in the ovarian tumor sample (Figure 1C; Table S1). For simplicity, only the top 5 differentially expressed genes are displayed. This is consistent with our previous work using bulk RNA-seq, which identified TREM2 as being associated with inhibitory TAMs but not stimulatory dendritic cell populations (Broz et al., 2014). We then assessed the fine distribution of TREM2 mRNA in TAMs, monocytes, and proliferating cells (which contain some TAMs) (Figure 1D) and found that, although a small proportion of monocytes have low-level TREM2 expression, almost all TAMs have significantly higher expression. Using the monocyte and TAM clusters from the ovarian scRNA-seq experiment as input cells for cell trajectory analysis (Trapnell et al., 2014), we demonstrated a progressive increase in TREM2 expression across the pseudotime trajectory (Figure 1E), with marked decreases and increases in monocyte- and macrophage-related genes, respectively (Figure S1A). Because enriched expression of a target is key for therapeutic development, we compared the expression of TREM2, CSF1R, and CD163 in normal tissue-resident macrophages (TRMs) and TAMs in breast (Castetta et al., 2019; Figure S1B). TREM2, compared with CSF1R or CD163, was substantially increased in TAMs compared with TRMs, indicating that TAMs are enriched for TREM2 on a per-

cell basis. We confirmed a per-cell increase in TREM2 on TAMs compared with TRMs using an independent scRNA-seq dataset in colorectal cancer (CRC), stomach adenocarcinoma (STAD), and uterine corpus endometrial carcinoma (UCEC) (data not shown; Cheng et al., 2021). To extend this analysis to more indications and a larger cohort, we analyzed TREM2 expression across 9,736 tumors and 8,587 normal samples from the The Cancer Genome Atlas (TCGA) and the Genotype Tissue-Expression (GTEx) projects (Figure S1C). We observed a consistent increase in TREM2 levels in tumors compared with normal tissue, further supporting tumor-enriched expression of TREM2. TREM2 has been identified previously as a determinant of TAM phenotype in the TME (Katzenelenbogen et al., 2020; Molgora et al., 2020) and disease recurrence (Obradovic et al., 2021), and we have previously found TREM2 expression to be correlated negatively with survival (Broz et al., 2014). We evaluated how expression of TREM2 in select human cancers from the TCGA dataset correlated with genes correlated with TAMs (*C1QC*) and TAM polarization (*MRC1* and *CD163*) (Figure S1D). In all comparisons, TREM2 was correlated significantly with TAM-associated genes.

To exhaustively examine the relationship of TREM2<sup>+</sup> TAM composition and T cell composition and status in the TME, we conducted scRNA-seq on CD45<sup>+</sup> tumor immune infiltrates from 10 different human tumors (Table S2) and aggregated the datasets to assess the transcriptional heterogeneity of myeloid cells (monocytes and macrophages), CD4<sup>+</sup> TILs, and CD8<sup>+</sup> TILs (Figure 2A; Figure S2A; Table S2). Cluster contribution from each sample was then assessed (Figures S2B and S2C). Aggregated sample analyses highlighted myeloid and lymphoid subclusters with unique transcriptional profiles, indicative of their phenotype or functional status, such as *PDGFB*-expressing (Kaneda et al., 2016) and *FOLR2*-expressing (Puig-Kröger et al., 2009) immunosuppressive TAMs (TAM C1 and TAM C2, respectively) and proliferating CD8<sup>+</sup> TILs (CD8<sup>+</sup> TIL – MKI67). Although TREM2 mRNA was observed across TAM, intermediate monocyte (Int. Mono), and monocyte clusters (Figures 2B and 2C), immunosuppressive TREM2<sup>+</sup> TAM C1 and TAM C2 comprised approximately 30% of the total monocyte and macrophage compartment (Figure 2D). We then performed a Pearson's r correlation analysis of the relative numbers of cells belonging to each myeloid subset with those derived from the CD4<sup>+</sup> TIL and CD8<sup>+</sup> TIL subclusters to ascertain potential myeloid-T cell relationships across the aggregated tumor set (Figure 2E; Table S3). Strikingly, the proportion of TREM2<sup>+</sup> TAM C1 and TAM C2 was highly correlated (0.65 and 0.39, respectively) with exhausted CD8<sup>+</sup> TILs (CD8<sup>+</sup> TIL – T<sub>EX</sub>), indicating that the presence of TREM2<sup>+</sup> immunosuppressive TAMs is indicative of an immunosuppressed and exhausted CD8<sup>+</sup> TIL component. The correlation of TREM2 and T cell exhaustion was extended and confirmed to occur on a per-sample basis using our individual human scRNA-seq samples (Figure S2D) as well as with select indications in TCGA (Figure 2F). Although recent work has identified a TREM2<sup>+</sup> immunosuppressive myeloid population subset in the mouse, designated Mreg (Katzenelenbogen et al., 2020), our analysis concluded that a transcriptionally equivalent population in humans is largely comprised of a mixed population of TAMs, Int. Monos, and monocytes (Figure S2E). This transcriptionally equivalent human

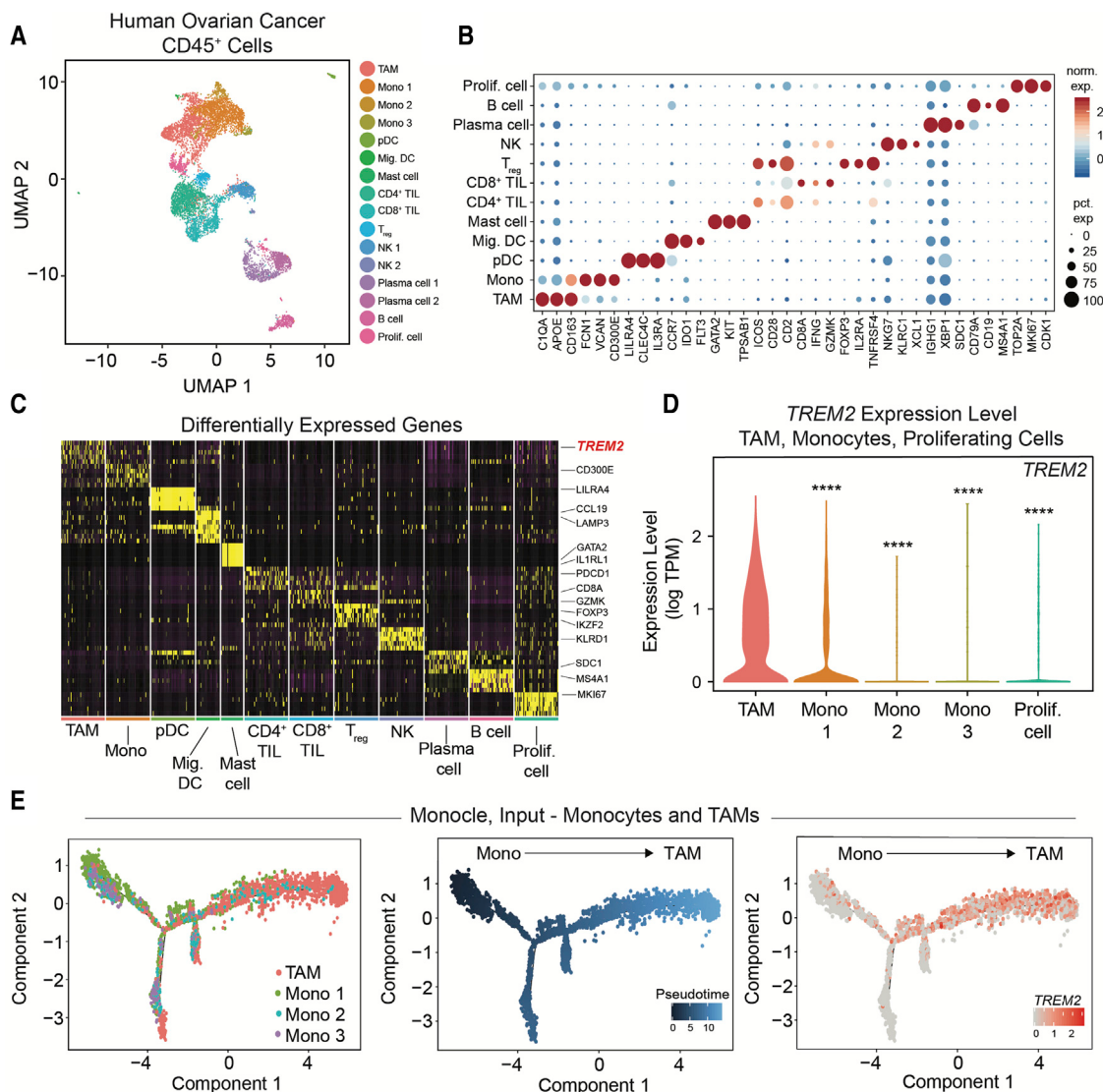


**Figure 1. TREM2 is expressed highly and specifically in human TAMs**

(A) Uniform manifold approximation and projection (t-SNE) plot and graph-based clustering of human CD45<sup>+</sup> tumor immune infiltrate from an ovarian tumor.

(B) Dot plot of cell type-identifying genes in identified cluster types. Cell types represented by multiple clusters were consolidated to simplify the plot (e.g., monocytes).

(C) Heatmap displaying the top differentially expressed genes between all clusters identified in (A). Differentially expressed genes for each cell type were filtered for those expressed in less than 10% of other cell types (Seurat percentage of cells where the feature is detected in the second group, i.e., pct.2 < 0.1). Cell types represented by multiple clusters were consolidated to simplify the analysis.

(D) Violin plot for TREM2 expression in select populations from (A). Wilcoxon rank-sum test was used for determining statistical significance.

(E) Monocle trajectory of monocytes and TAMs, displaying cell types (left), pseudotime (center), and TREM2 levels (right).

See also Figure S1 and Table S1.

population did not correlate strongly with exhausted CD8<sup>+</sup> TILs, in contrast to the TREM2<sup>+</sup> TAM C1 and TAM C2 populations identified in our work.

To extend our findings to a highly tractable system with innate PD-1 resistance, we utilized the CT26 syngeneic mouse tumor model (Efremova et al., 2018; Lau et al., 2017). Flow cytometry (Figure 3A; Figure S3E) and 10X Genomics scRNA-seq (Figures S3A–S3D; Table S4) of CD45<sup>+</sup> immune cells from dissociated CT26 tumors demonstrated that, similarly to humans, TREM2

is specific to TAMs in this mouse TME. Additionally, we assessed the frequency of TREM2<sup>+</sup> TAMs in the CT26 and EMT6 tumor models and found that, on average, tumors ranging between 100–300 mm<sup>3</sup> had less than 50% of TAMs being TREM2<sup>+</sup> (Figure S3F).

To address how TREM2 expression changes as a function of tumor progression and TME immunosuppression, we analyzed expression of TREM2 on CD64<sup>+</sup> F4/80<sup>+</sup> TAMs in tumors of increasing size, finding a clear pattern of increasing TREM2

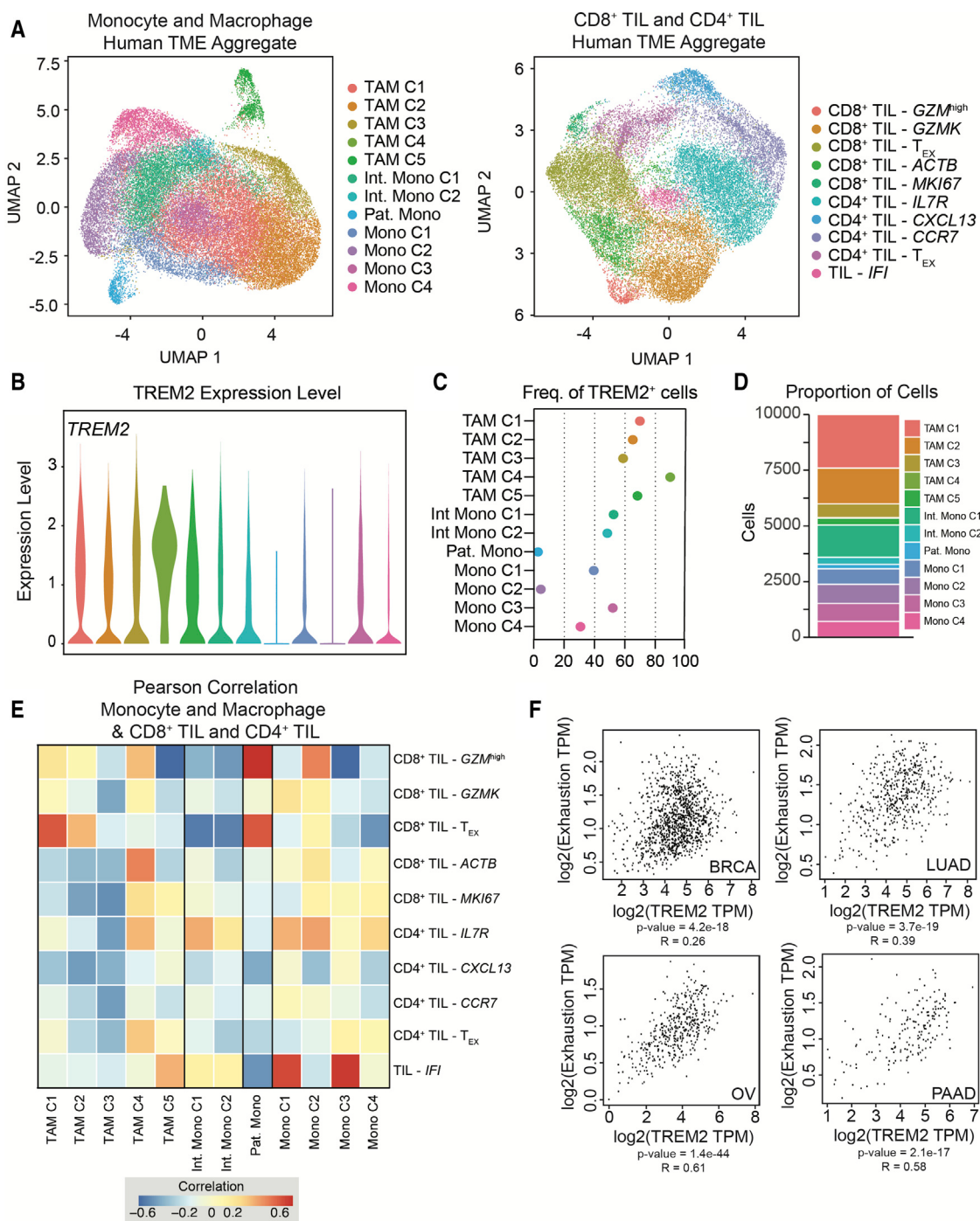


**Figure 2. TREM2<sup>+</sup> immunosuppressive TAMs are correlated with an exhausted T cell state in the human TME**

(A) UMAP plots of monocytes and macrophages (left) or CD4<sup>+</sup>/CD8<sup>+</sup> TILs (right) from 10 individuals' aggregated CD45<sup>+</sup> immune infiltrate.

(B) Violin plots displaying expression probability differences for TREM2 in monocyte and macrophage clusters from (A).

(C) Frequency of TREM2<sup>+</sup> myeloid cells in transcriptionally distinct clusters.

(D) Proportion of monocytes and macrophages comprised of each cluster from 10,000 randomly sampled cells from (A).

(E) Heatmap of Pearson correlation R values generated from the cell sample fractions in each cluster comparison (relates to A). Pearson correlation R values were constructed by comparing the per-tumor number of cells derived from each myeloid subcluster with all CD4<sup>+</sup> TIL and CD8<sup>+</sup> TIL counterparts. Each tile in the heatmap is colored by the resultant correlation value across all aggregated tumors. Significance for each comparison was computed via Monte Carlo permutation.

(legend continued on next page)

levels correlating with progression (Figure 3B). To understand how tumor burden, TREM2 expression levels, and T cell exhaustion correlate, we analyzed the levels of the T cell exhaustion markers thymocyte selection associated high mobility group box (TOX) and PD-1 on CD8<sup>+</sup> TILs in tumors of increasing size (Figure 3C). This analysis demonstrated a marked increase in TOX<sup>+</sup> PD-1<sup>+</sup> CD8<sup>+</sup> TILs in more advanced, immunosuppressed tumors (Figure 3D). When we treated CT26 tumor-bearing mice (Figure 3E) and assessed TREM2 surface levels on TAMs (Figure 3F) and TREM2<sup>+</sup> TAM numbers in the TME (Figure 3G), we found that both increased with anti-PD-1 antibodies, although the magnitude did not meet statistical significance compared with control antibodies. Our data indicate that TREM2 is enriched on TAMs and that a TREM2<sup>+</sup> TAM-rich TME is immunosuppressive and could be a contributing factor in initiating or maintaining resistance to anti-PD-1 treatment.

#### Fc domain-enhanced anti-TREM2 mAb treatment sensitizes anti-PD-1-resistant tumors

Based on the expression pattern of TREM2 and its putative relationship to tumor progression and CD8<sup>+</sup> TIL exhaustion, we hypothesized that therapeutically targeting and skewing the proportion of TREM2<sup>+</sup> TAMs through depletion to rebalance the immune infiltrate would benefit anti-tumor immune responses. To promote depletion of TREM2<sup>+</sup> target cells, we designed two anti-TREM2 mAbs that were Fc competent (anti-TREM2-wild type [WT]) or Fc effector enhanced (anti-TREM2), differing only in their core fucosylation state (Houde et al., 2010). As expected, we did not observe any differences between the two antibodies in their ability to bind TREM2 antigen expressed on the cell surface (Figure S4A). Although fucosylated anti-TREM2-WT and afucosylated anti-TREM2 mAbs demonstrated comparable antibody-dependent cellular phagocytosis (ADCP) of TREM2<sup>+</sup> target cells compared with isotype controls (Figure 4A; Figures S4B and S4C), afucosylated anti-TREM2 mAbs elicited superior antibody-dependent cellular cytotoxicity (ADCC) compared with fucosylated anti-TREM2-WT (Figure 4B; Figure S4D). Anti-TREM2 induced ADCC when IL-4-elicted primary bone marrow-derived macrophages (BMDM)-expressing endogenous levels of TREM2 were used as cellular targets (Figure S4E).

To determine whether targeting of TREM2<sup>+</sup> TAMs elicited anti-tumor immunity independent of anti-PD-1 treatment, we treated mice harboring anti-PD-1 sensitive syngeneic EMT6 subcutaneous tumors with the anti-TREM2 mAb (Figure 4C; Figure S4F). Compared with isotype mAb treatment, anti-TREM2 mAb treatment resulted in pronounced control of tumor growth. Because the anti-TREM2 mAb is designed to eliminate TREM2<sup>+</sup> TAMs, we next investigated whether TAM abundance was affected following anti-TREM2 mAb treatment (Figure 4D). Anti-TREM2 mAb treatment progressively enabled a marked reduction in the proportion of TAMs, indicating that an afucosylated anti-TREM2 mAb depleted TREM2<sup>+</sup> TAMs in the TME, consistent with the ability of anti-TREM2 mAbs to mediate ADCC *in vitro*. To investigate the pharmacokinetic properties of anti-TREM2

therapy on endogenous TREM2, we analyzed TREM2 receptor occupancy (RO) and total TREM2 receptor levels on BMDMs and TAMs following *in vitro* (Figure S4G) and *in vivo* (Figure S4F) treatment with anti-TREM2. In both instances, anti-TREM2 treatment contributed to partial RO, but interpretation is complicated by the substantial increase in total TREM2 induced by anti-TREM2 therapy.

#### The anti-TREM2 mAb potentiates activation of intratumoral CD8<sup>+</sup> T cells in an anti-PD-1 resistant tumor model

We next investigated whether therapeutic targeting of TREM2<sup>+</sup> TAMs reversed anti-PD-1 resistance in the CT26 subcutaneous tumor model (Figure 5A). Although neither anti-PD-1 nor anti-TREM2 mAbs had appreciable anti-tumor activity as single-agent treatments, simultaneous anti-PD-1 and anti-TREM2 mAb treatment enabled pronounced control of tumor growth. A cohort of mice (20%–60% in different studies) was able to completely eliminate CT26 subcutaneous tumors and remain tumor free for over a month following cessation of the combination anti-PD-1 and anti-TREM2 mAb therapy. Such complete responders were rechallenged with CT26 tumor cells after a treatment-free holiday period. No palpable tumor growth occurred in these rechallenged mice, demonstrating that the anti-tumor immunity of anti-PD-1 and anti-TREM2 mAb treatment generated immune memory (Figure 5B).

Based on our findings, we hypothesized that anti-TREM2 treatment potentiates response to anti-PD-1 treatment by eliciting CD8<sup>+</sup> TIL-driven anti-tumor immunity. To test this, we treated CT26 tumor-bearing animals with isotype mAbs, anti-PD-1, anti-TREM2, or a combination of anti-PD-1 and anti-TREM2 mAbs and then performed a series of analyses to systematically assess the microenvironment in the tumor. We first analyzed the proportion of CD8<sup>+</sup> TILs in the TME of treated mice (Figure S5A). Consistent with our hypothesis, there was a modest but non-significant increase in CD8<sup>+</sup> TILs observed only with combination therapy. We also quantitatively assessed CD8<sup>+</sup> TIL infiltration by CD8α immunohistochemistry (IHC) and found that combination treatment significantly increased the numbers of CD8<sup>+</sup> TILs in the TME (Figure S5B), with a less pronounced effect from anti-PD-1 monotherapy. To understand whether combination treatment affected the transcriptional profile of CD45<sup>+</sup> immune cells, we performed scRNA-seq on CD45<sup>+</sup> immune infiltrate from CT26 tumor-bearing mice treated with isotype, anti-PD-1, anti-TREM2, or anti-PD-1 and anti-TREM2 mAbs. scRNA-seq datasets from each condition were aggregated and analyzed in a manner consistent with the untreated CD45<sup>+</sup> immune infiltrate from CT26 tumor cells shown in Figure 1. After isolating lymphoid cells from the dataset and reclustering (22,081 cells in total), we identified 14 clusters that were represented by all treatment groups (Figures S5C–S5E). Any cluster with co-expression of canonical lymphoid and myeloid genes were labeled as “MyL/Lym combined” and excluded from further analysis (Figure S5F).

(F) Correlation between TREM2 expression and T cell exhaustion signature in human breast cancer (BRCA), lung adenocarcinoma (LUAD), ovarian cancer (OV), and pancreatic adenocarcinoma (PAAD) samples from the TCGA dataset.

See also Figure S2 and Tables S2 and S3.

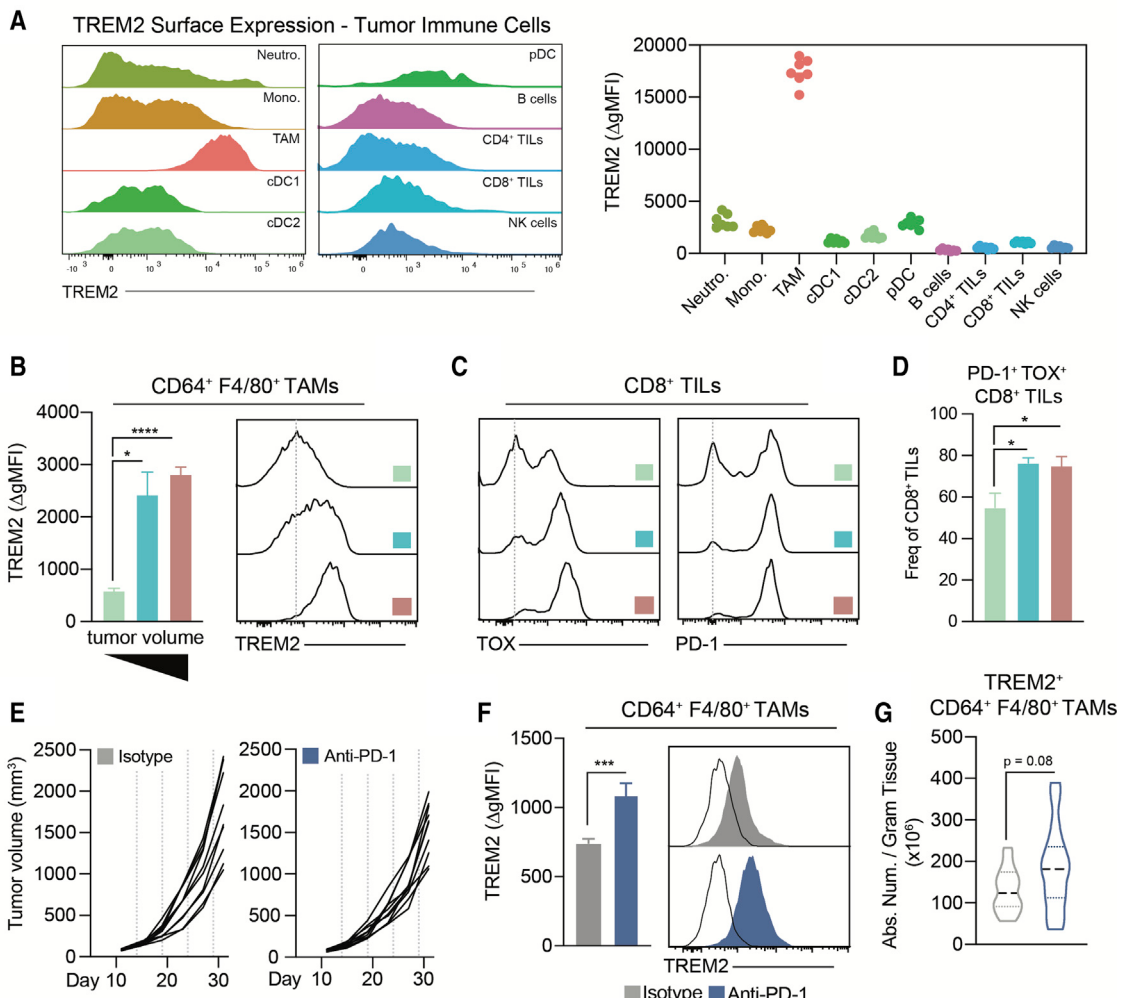


**Figure 3. TREM2 expression correlates with tumor size and anti-PD-1 resistance in mouse**

(A) Representative histograms from flow cytometry data of TREM2 levels on intratumoral myeloid (left) and lymphoid cells (right).  
 (B) TREM2 surface levels on TAMs at different tumor volumes (left) with representative histograms (right) ( $n = 6/\text{group}$ ).  
 (C) Representative histograms of intracellular TOX (left) and surface PD-1 (right) on CD8<sup>+</sup> TILs at different tumor volumes.  
 (D) Frequency of CD8<sup>+</sup> TILs that are PD-1<sup>+</sup> TOX<sup>+</sup> at different tumor volumes ( $n = 5/\text{group}$ ). X-axes as seen in (B).  
 (E) Tumor growth from CT26 tumor-bearing mice treated with isotype (left) or anti-PD-1 (right). Vertical dotted lines indicate days of treatment.  
 (F) TREM2 surface levels on TAMs 2 days after the second dose of isotype or anti-PD-1 (left) and representative histograms (right). Unpaired t test was performed.  
 (G) The absolute number normalized to tissue weight of TREM2<sup>+</sup> TAMs 2 days after the second dose of isotype or anti-PD-1.

Unless specified otherwise, all experiments were performed two or more times. For graphs with error bars, mean  $\pm$  SEM is shown. \* $p < 0.05$ , \*\* $p < 0.01$ , \*\*\* $p < 0.001$ , \*\*\*\* $p < 0.0001$ . See also Figure S3 and Table S4.

Consistent with our transcriptional observations, we also found an increased abundance of interferon  $\gamma$  (IFN $\gamma$ ) and tumor necrosis factor alpha (TNF- $\alpha$ )-producing CD8<sup>+</sup> TILs in the TME of combination-treated mice (Figure 5C). IFN $\gamma$  and TNF- $\alpha$  protein levels as well as IL-12p70 and IL-15 levels were enriched in supernatants from tumors of mAb-treated animals (Figure 5D). Because expression of individual genes can provide a selective view of a cellular state, we wanted to understand how transcription from a broader, holistic level was affected. Thus, we performed a gene set enrichment analysis (GSEA) comparing CD8<sup>+</sup> TILs from isotype-treated and combination anti-PD-1 and anti-TREM2 mAb-treated mice. We observed that combina-

tion-treated CD8<sup>+</sup> TILs displayed a significant increase in the IFN $\gamma$  response pathway (normalized enrichment score, 2.128; adjusted  $p = 0.010$ ) and TNF- $\alpha$  signaling via the nuclear factor  $\kappa$ B (NF- $\kappa$ B) pathway (normalized enrichment score, 2.477; adjusted  $p = 0.010$ ) (Figure 5E; Table S5). We also observed that CD8<sup>+</sup> TILs from combination-treated mice had enrichment of glycolysis-related genes and a decrease in genes involved in oxidative phosphorylation, consistent with studies that show higher glycolysis in effector populations (Geltink et al., 2018). Additionally, GSEA comparing CD8<sup>+</sup> TILs from anti-PD-1 and combination of anti-PD-1 and anti-TREM2 generated a complement of pathways (Table S5) similar to the prior analysis.

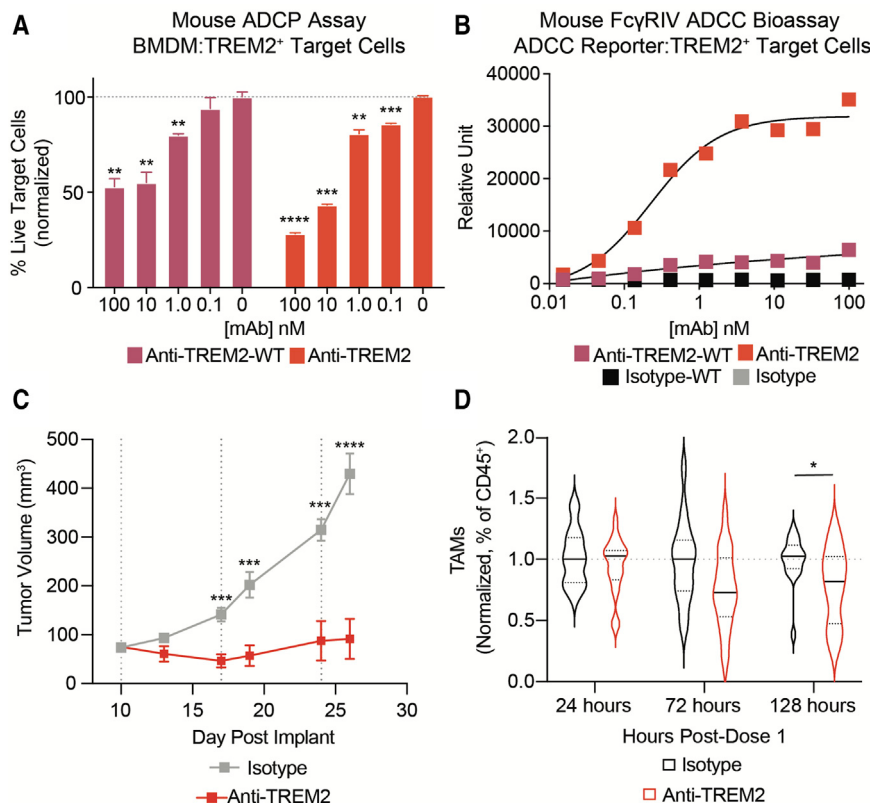


**Figure 4. Fc effector-enhanced anti-TREM2 mAb therapy reverses anti-PD-1 resistance**

(A) Frequency of live TREM2<sup>+</sup> target cells following co-culture with mouse BMDMs and varying amounts of anti-TREM2-WT (mouse immunoglobulin G2a [IgG2a]) or anti-TREM2 (afucosylated mouse IgG2a) ( $n = 4$ /group). Samples were combined from two independent experiments.

(B) ADCC reporter cell fluorescence following co-culture with or ADCC reporter cells and TREM2<sup>+</sup>-expressing target cells and varying amounts of anti-TREM2-WT, anti-TREM2, or appropriate isotypes ( $n = 2$ /group).

(C) Tumor growth of EMT6-tumor bearing animals treated with 5 mg/kg of isotype or anti-TREM2. Vertical dotted lines indicate days when mAb dosing occurred ( $n = 10$ /group).

(D) Violin plots of intratumoral normalized TAMs as a frequency of CD45<sup>+</sup> cells from isotype- and anti-TREM2-treated EMT6 tumor-bearing mice 24, 72, and 128 h after mAb treatment. Samples were combined from two independent experiments (experiment 1,  $n = 4$ –7/group; experiment 2,  $n = 10$ /group).

Unless specified otherwise, all experiments were performed two or more times. For graphs with error bars, mean  $\pm$  SEM is shown. \* $p < 0.05$ , \*\* $p < 0.01$ , \*\*\* $p < 0.001$ , \*\*\*\* $p < 0.0001$ . See also Figure S4.

CD8<sup>+</sup> TILs in combination-treated mice were found to have the highest expression levels of effector T cell-related genes, such as *Ifng*, *Ly6c1*, *Tbx21*, and *Eomes* (Figure 5F; Table S6). We also observed expression of genes with a reported inhibitory role, such as *Lag3*, *Ctla4*, and *Havcr2*. These findings are consistent with previous observations that CD8<sup>+</sup> TILs begin to express higher levels of activation-induced genes meant to subsequently dampen inflammation in a self-controlled manner (Agata et al., 1996; Walunas et al., 1994). These data support that anti-TREM2 treatment potentiates anti-PD-1 sensitivity and anti-PD-1-induced CD8<sup>+</sup> TIL activation.

#### Anti-TREM2 mAb treatment induces profound changes in the tumor myeloid compartment

Based on our findings demonstrating TAM depletion following anti-TREM2 mAb treatment and potent activation of CD8<sup>+</sup> TILs following combination anti-TREM2 and anti-PD-1 mAb treatment, we hypothesized that combination treatment would elicit changes in the proportion and phenotype of TAMs in the mouse TME. Thus, we assessed changes in immune composition and gene expression in tumors following mAb treatment. In agreement with anti-TREM2 mAbs being ADCC competent, single-agent anti-TREM2 mAb and combination anti-TREM2 and anti-PD-1 mAb treatment resulted in a reduction of CD64<sup>+</sup> F4/80<sup>+</sup> TAMs and an increase in neutrophils in the TME (Figure 6A). We suspected that the effect of depletion was partially masked by infiltration of new myeloid cells, and in line with that, levels of myeloid-attracting chemokines, such as MIP-1 $\alpha$  and MCP-1, were increased following combination

treatment (Figure S6A). Upon further investigation, we found that major histocompatibility complex (MHC) class II<sup>−</sup> TAMs, which are thought to be more M2 like (Xiong et al., 2019), expressed higher levels of TREM2 (Figure 6B) and were selectively reduced by combination therapy (Figure 6C). Although a reduced proportion of M2-like TAMs would benefit anti-tumor immunity, we investigated whether there were transcriptional changes in the remaining TAMs following combination treatment. To focus our analysis on the myeloid compartment, myeloid cells (25,503 in total) identified in the scRNA-seq experiment, as described in Figure 4, were isolated and reclustered, yielding 12 clusters comprised of cells from all treatment conditions (Figures S6B–S6D). Similar to aggregation of lymphoid cells, clusters with co-expression of canonical lymphoid and myeloid cells were labeled “MyL/Lym combined” and excluded from further analysis (Figure S6E). We then assessed the scale and breadth of expression of known pro- and anti-inflammatory macrophage genes in TAMs across the four treatment conditions (Figure 6D; Table S7). We observed enhanced expression of pro-inflammatory genes in the residual TAMs following combination treatment. In addition to upregulation of pro-inflammatory genes, we observed increased expression of the M2-associated gene *Arg1* in combination-treated TAMs, an effect seen previously by others (Gubin et al., 2018). Consistent with a more pro-inflammatory phenotype, TAMs from combination-treated tumors displayed increased expression of the co-stimulatory or activation-induced surface markers CD40 and CD86 (Figure 5E; Chen and Flies, 2013). Anti-TREM2 and anti-PD-1 mAb combination treatment induces

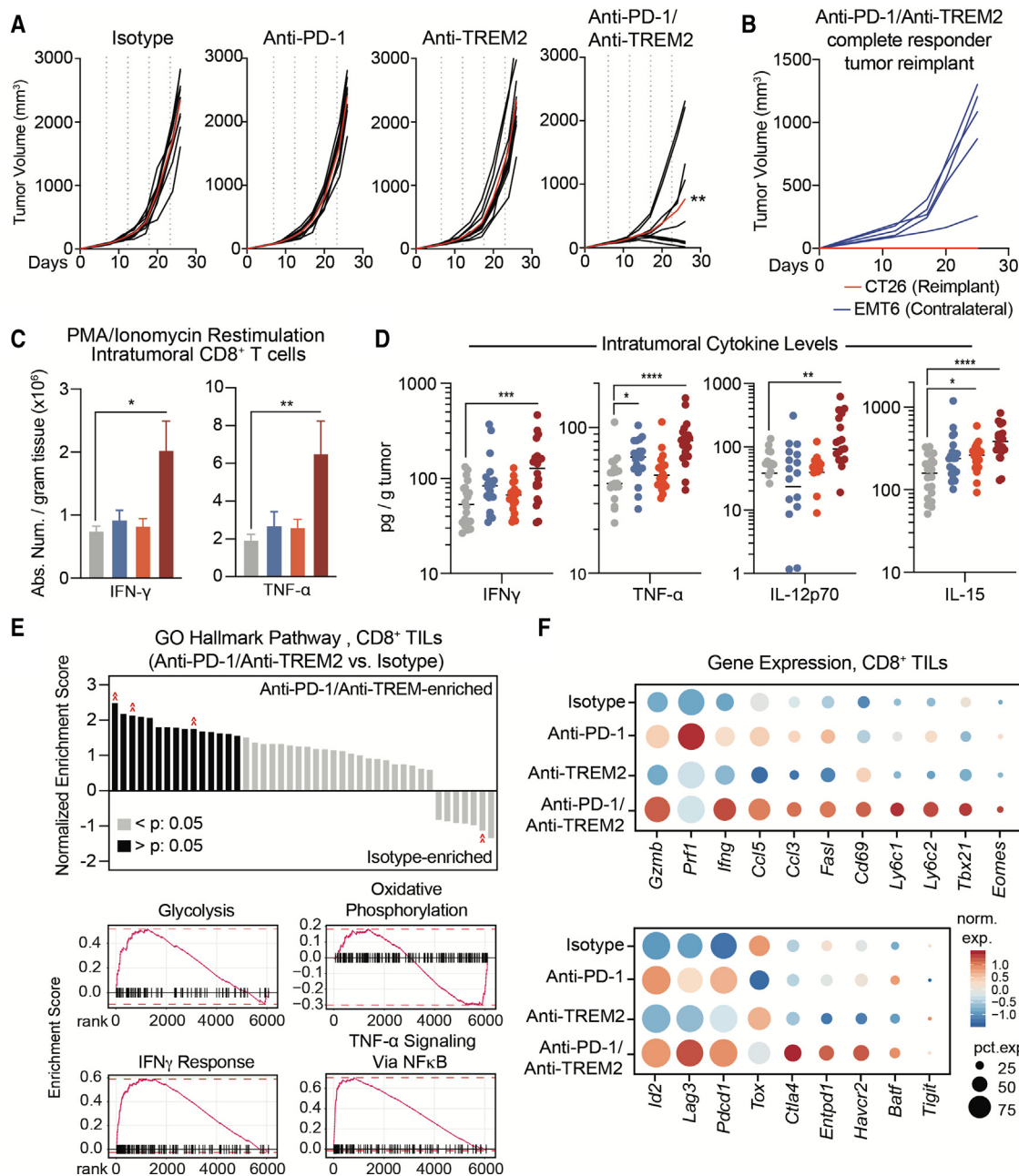


**Figure 5. Anti-PD-1 and anti-TREM2 mAbs synergize to promote effector T cell function and remodel the TAM compartment**

(A) Tumor growth of CT26-tumor bearing animals treated with isotype, anti-PD-1, anti-TREM2, or anti-PD-1 and anti-TREM2 mAbs. Red lines indicate average tumor volume, and dotted lines indicate points of treatment. Group comparisons for tumor volume (day 28) were conducted using Mann-Whitney U test.

(B) Tumor rechallenge experiment of CT26-tumor bearing mice that were treated previously with anti-PD-1 and anti-TREM2 mAbs and displayed complete response. Red lines are from CT26 reimplanted tumors, and blue lines are from EMT6 tumors injected on the contralateral flank.

(C) Quantified absolute number per gram tissue ( $\times 10^6$ ) of IFN $\gamma$ <sup>+</sup> (left) and TNF- $\alpha$ <sup>+</sup> (right) CD8<sup>+</sup> T cells following phorbol 12-myristate 13-acetate (PMA)/ionomycin restimulation ( $n = 9-10$ ).

(D) Intratumoral cytokine analysis of IFN $\gamma$ , TNF- $\alpha$ , IL-12p70, and IL-15 ( $n = 15/\text{group}$ ). Mean value of the group is displayed.

(E) Gene Ontology (GO) hallmark pathway analysis of CD8<sup>+</sup> TILs, comparing isotype and anti-PD-1 and anti-TREM2 mAbs. Top: graph of enriched pathways. Bottom: red chevrons indicate highlighted pathways displayed.

(F) Dot plot of gene expression within isotype-, anti-PD-1-, anti-TREM2-, and anti-PD-1/anti-TREM2-treated CD8<sup>+</sup> T cells for effector T cell-related and activation-induced genes.

Unless specified otherwise, all experiments were performed two or more times. \* $p < 0.05$ , \*\* $p < 0.01$ , \*\*\* $p < 0.001$ , \*\*\*\* $p < 0.0001$ . See also Figure S5 and Tables S5 and S6.

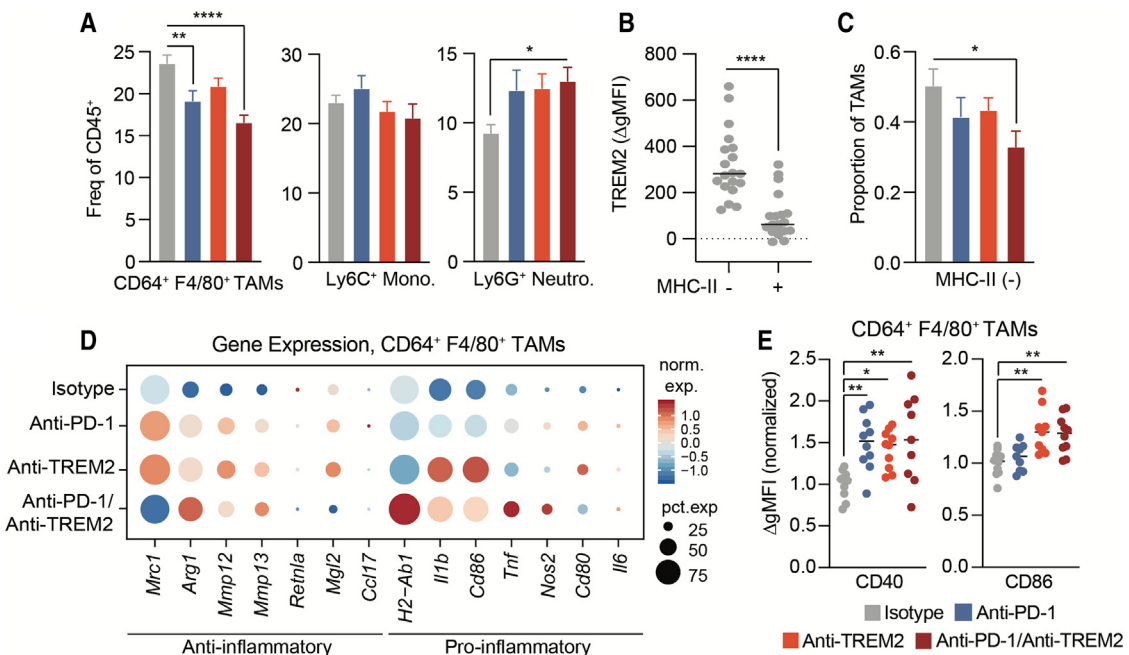


**Figure 6. Anti-TREM2 mAb therapy remodels the TAM compartment**

(A) Flow cytometry proportion of CD64<sup>+</sup> F4/80<sup>+</sup> TAMs, Ly6C<sup>+</sup> monocytes, and Ly6G<sup>+</sup> neutrophils as a frequency of CD45<sup>+</sup> tumor immune cells (n = 15).  
 (B) Flow cytometry analysis of TREM2 surface levels on MHC class II<sup>-</sup> and MHC class II<sup>+</sup> TAMs (n = 19).  
 (C) The proportion of TAMs that are MHC class II<sup>-</sup> following mAb treatment (n = 10).  
 (D) Dot plot of gene expression in isotype-, anti-PD-1-, anti-TREM2- and anti-PD-1- and anti-TREM2-treated TAMs for myeloid-focused pro- and anti-inflammatory genes.  
 (E) Cell surface levels of CD40 (left) and CD86 (right) on CD64<sup>+</sup> F4/80<sup>+</sup> TAMs from tumors of mAb-treated animals (n = 9–10). Color legends aligned with (A) and (C). Mean value of each group is displayed. Unless specified otherwise, all experiments were performed two or more times. \*p < 0.05, \*\*p < 0.01, \*\*\*p < 0.001, \*\*\*\*p < 0.0001. See also Figure S6 and Table S7.

pronounced effects on TAMs in the TME, including proportional changes indicative of selective depletion of M2-like TAMs as well as phenotypic alterations in the residual TAMs toward a pro-inflammatory phenotype.

#### Ovarian cancer is TREM2 rich and may benefit from anti-TREM2 mAb therapeutic intervention

To understand the scale and distribution of TREM2 surface expression on myeloid cells in the human TME, we performed flow cytometric analysis on 49 dissociated human tumor samples from distinct cancer indications (Figure 7A; Figure S7A). Extending and confirming our scRNA-seq analyses, TREM2 protein was expressed primarily on TAMs compared with all other analyzed myeloid populations. To identify indications that are TREM2- and TAM-rich, we extended this analysis by comparing the scale of TREM2 surface levels on TAMs and the proportion of TAMs in the TME (Figure 7B). Of all analyzed indications, ovarian cancer was the most TREM2 and TAM rich, with 4 of 9 tumor samples having a TREM2 geometric mean fluorescence intensity (gMFI) above 1,000 and TAMs representing more than 10% of the CD45<sup>+</sup> immune infiltrate.

Ovarian cancer has so far demonstrated a modest response to CPI therapy (Matulonis et al., 2019). To understand how TREM2<sup>+</sup> TAMs change with progression of ovarian cancer, we used IHC to analyze TREM2 expression in human ovarian cancer with

increasing stages of disease severity (Figure 7C; Figure S7B). We found that, although a TREM2 H-score (a cumulative measure of receptor frequency and staining intensity) was low on normal ovaries, the TREM2 H-score increased steadily beginning at stage 1 through stage 3 of ovarian cancer. This phenomenon was also largely confirmed in liver and colon cancer (Figure S7C). Next, to address the relationship of TREM2 expression in individuals with ovarian cancer and disease outcome, we utilized a dataset that contained gene expression and recurrence-free survival from 285 individuals with ovarian cancer (Tothill et al., 2008). Analysis of upper- and bottom-quartile TREM2 gene expression and recurrence-free survival from 285 individuals with ovarian cancer (Tothill et al., 2008) showed worse recurrence-free survival of individuals with the highest TREM2 expression (Figure 7D). These data are consistent with TREM2<sup>+</sup> TAMs being central mediators in driving an immunosuppressed TME as disease grade worsens.

To extend our findings to a tractable model, we tested whether the orthotopic syngeneic ovarian cancer model, ID8<sup>Luc2</sup>, would respond to anti-TREM2 mAb treatment (Figures 7E and 7F). Although isotype mAb-treated mice had progressive disease, mice treated with anti-TREM2 mAbs demonstrated a reduced tumor burden. These data indicate that individuals with a highly immunosuppressive TREM2<sup>+</sup> TAM-rich TME, such as those with ovarian cancer, could benefit from therapy with an antibody that targets TREM2<sup>+</sup>-expressing TAMs.

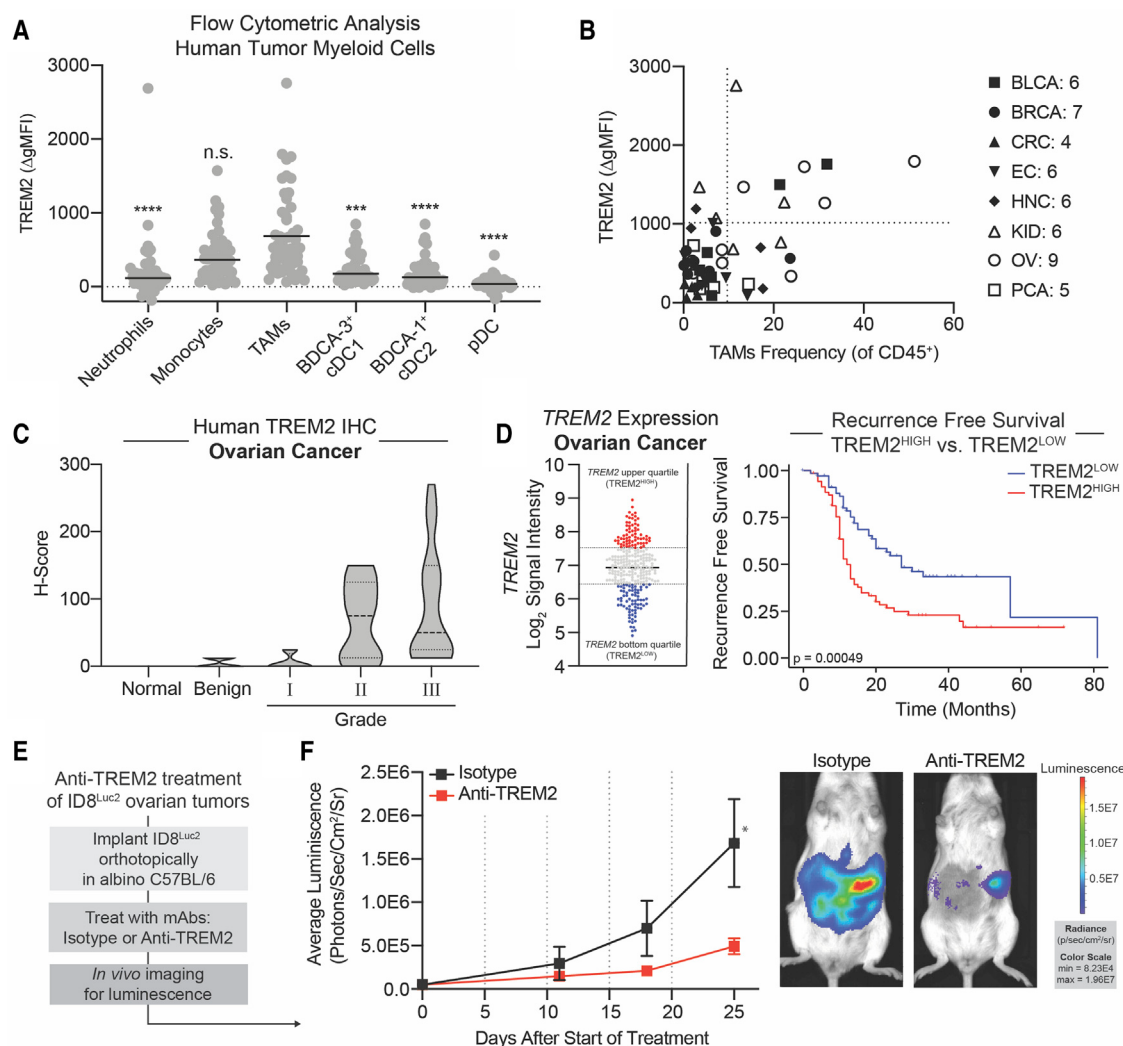


**Figure 7. OV is TREM2 rich and might benefit from anti-TREM2 mAb therapeutic intervention**

(A and B) Flow cytometry analysis of the human TME ( $n = 49$ ) detailing TREM2 surface expression ( $\Delta gMFI = gMFI^{\text{TREM2}} - gMFI^{\text{Isotype}}$ ) on myeloid populations with group mean value displayed (A) or comparing TREM2  $\Delta gMFI$  with TAM density as a frequency of CD45 $^{+}$  immune cells (B). For statistical comparison in (A), Dunn's multiple comparisons test was performed with individual groups tested versus TAMs. BLCA, bladder cancer; CRC, colorectal cancer; EC, endometrial cancer; HNC, head and neck cancer; KID, kidney cancer; PCA, prostate cancer.

(C) TREM2 IHC H-score from normal human ovarian tissue, benign ovarian growths, and OV grades I, II, or III.

(D) Analysis of an OV dataset that contained expression data and recurrence-free survival data. Individuals in the upper and lower quartile of TREM2 mRNA expression were identified (left) and assessed for recurrence-free survival (right).

(E) Experimental schematic for (F).

(F) C57BL/6 mice were implanted orthotopically with ID8-Luc cells and subsequently treated with isotype or anti-TREM2 mAb ( $n = 10/\text{group}$ ). Vertical dotted lines indicate days of mAb treatment. Comparisons were made using Mann-Whitney  $U$  test. Representative luminescence images of isotype and anti-TREM2 mAb treated ID8<sup>Luc2</sup> tumor bearing mice are shown.

For graphs with error bars, mean  $\pm$  SEM is shown. Unless specified otherwise, all experiments were performed two or more times. \* $p < 0.05$ , \*\* $p < 0.01$ , \*\*\* $p < 0.001$ , \*\*\*\* $p < 0.0001$ . See also Figure S7.

## DISCUSSION

Here we described TREM2 as a TAM-enriched target in CPI-resistant human and mouse TMEs and demonstrate that therapeutic targeting of TREM2 with Fc domain effector-enhanced antibodies can drive productive antitumor immunity in tumors that are otherwise resistant to CPI therapy. Our work is relevant to current and future clinical efforts focused on identifying

orthogonal therapeutic modalities that will synergize, enhance, and enable existing CPI therapies.

Although the relationship between TREM2 and immunosuppression in the context of the TME has been investigated previously (Katzenellenbogen et al., 2020; Molgora et al., 2020), much of what is known about TREM2 and its role in inflammation has been drawn from studies of microglia and the central nervous system. TREM2 in microglia promotes phagocytosis

of apoptotic neurons, and, through its association with DAP12, it can downregulate transcription of pro-inflammatory genes like *Tnfa*, *Il1b*, and *Nos2* (Takahashi et al., 2005). By extending this to the context of the TME, where apoptotic cell products are common and TAMs are abundant, it seems likely that TREM2 would promote a chronic immunosuppressive state in TAMs, in turn contributing to a broadly immunosuppressive immune milieu and ultimately driving CPI resistance.

In the case of human cancer, where access to tissues is a limiting factor, scRNA-seq can be utilized for its unbiased and high-dimensional assessment of broad cell-type-specific expression analysis. With a relatively small cell number input, we were able to clearly demonstrate *TREM2* as being human TAM enriched. Although *TREM2* expression has been noted previously on human TAMs (Katzenellenbogen et al., 2020; Lavin et al., 2017; Molgora et al., 2020), our analyses enabled highly granular assessments of the distribution of *TREM2* expression in myeloid populations and the effect of *TREM2*<sup>+</sup> TAMs on the prevalence of activated or exhausted T cells in the human TME.

This correlative evidence from human tumor samples was complemented by functional preclinical evidence of *TREM2*-mediated immunosuppression in tumors using the anti-PD-1-resistant mouse tumor model CT26. We found that disease severity correlated with an increase in *TREM2* expression, which corresponded to more pronounced T cell exhaustion. Failed anti-PD-1 therapy elicited higher surface *TREM2* on TAMs and a trending increase in *TREM2*<sup>+</sup> TAMs, highlighting the potential role of *TREM2* and *TREM2*<sup>+</sup> TAMs in immunosuppression and promotion of tumor growth.

Therapeutic reduction of TAMs through blockade of monocyte or macrophage chemoattraction in the case of the CCL2 and CCR2 axis or differentiation with CSF-1 and CSF-1R has been attempted in pre-clinical and clinical settings with unproven success (Jahchan et al., 2019). We reasoned that the restricted expression profile on TAMs and putative role of *TREM2* in immunosuppression would make it an optimal target for development of afucosylated, effector-enhanced antibodies that could elicit ADCC- or ADCP-mediated TAM elimination. N-linked glycosylation in the Fc region of antibodies has a profound effect on the capacity of an antibody to mediate ADCC through its interaction with Fc $\gamma$ R on effector populations. Through use of glycoengineering, minimization or abrogation of fucose on Fc N-glycans can yield antibodies with improved capability to elicit ADCC at relatively lower antibody concentrations (Yamane-Ohnuki and Satoh, 2009). Consistent with the work of others (Shields et al., 2002), our core afucosylated Fc domain effector-enhanced anti-*TREM2* mAb outperformed the anti-*TREM2* fully fucosylated mAb in ADCC and ADCP, enabling us to perform paired efficacy and pharmacodynamic testing with the anti-*TREM2* mAb as a single agent, where we observed pronounced antitumor activity and depletion of TAMs in the TME.

Our data and prior work suggested that *TREM2* functions as an innate immune resistance mechanism in response to failed anti-PD-1 therapy. To understand whether anti-*TREM2* mAb therapy might enhance the response to anti-PD-1, we employed the anti-PD-1-resistant CT26 tumor model. We only observed efficacy when anti-PD-1 and anti-*TREM2* mAbs were combined

and, thus, hypothesized that anti-*TREM2* mAb therapy potentiated anti-PD-1 response through enhanced T cell infiltration or activation and modulation of TAM composition. In the pharmacodynamic analysis, we observed that CD8+ T cells were more abundant within the TME and that they produced higher amounts of effector cytokines and that their activation state, determined through transcriptional analysis, was improved. Consistent with anti-*TREM2* mAb being an effector-enhanced antibody, we found that productive anti-*TREM2* mAb therapy elicited a significant reduction in TAMs in the EMT6 and CT26 tumor models. In no instance did we observe a total reduction in TAMs, suggesting that, in addition to depletion, there may be alternative mechanisms of action that benefit antitumor immunity. Although the overall decrease in TAMs was moderate, we believe that production of myeloid-attracting chemokines (Figure 6) increases *de novo* infiltration and differentiation of M1-like TAMs, as evidenced by the increases in abundance of MHC class II<sup>+</sup> TAMs and enhanced pro-inflammatory gene expression. The absence of robust depletion as a single agent in the CT26 model requires further analysis, but we suspect that it involves inadequate ADCC- or ADCP-capable effector populations when treated with anti-*TREM2* mAbs alone. Furthermore, our data cannot exclude the possibility that our antibody blocks the normal immunosuppressive function of *TREM2* and, in doing so, potentiates antitumor immunity.

Previous work using IHC has demonstrated that *TREM2*<sup>+</sup> cells are abundant and highly prevalent in the human TME (Molgora et al., 2020). To expand these findings, we performed multiparametric flow cytometry on dissociated tumor immune cells from 50 human tumor samples in which we assessed *TREM2* expression across common myeloid populations. As expected, based on our scRNA-seq data, TAMs had higher *TREM2* surface levels than the other analyzed myeloid populations across all tested tumor types. Because our data demonstrated that ovarian cancer had the largest average proportion of *TREM2*<sup>+</sup> TAMs within our flow cytometry dataset, we used this indication for a more detailed analysis. We observed that, as ovarian cancer grade becomes more severe, a marked increase in *TREM2* levels is detectable via IHC. This grade-specific increase in *TREM2* was also observed in liver cancer and, to a lesser extent, in colon cancer. Consistent with the relationship between *TREM2*<sup>+</sup> TAMs and disease grade severity, *TREM2* expression levels were correlated inversely with recurrence-free survival in ovarian cancer. A central feature of the CPI resistance in ovarian cancer might be related to a highly immunosuppressed TME as a result of abundant of *TREM2*<sup>+</sup> TAMs. To determine whether anti-*TREM2* mAb therapeutic intervention might benefit ovarian cancer, we employed the ID8<sup>Luc2</sup> orthotopic ovarian cancer model. Strikingly, as single-agent therapy, the anti-*TREM2* mAb was able to drive a robust antitumor response in this model. These data highlight not only the critical suppressive axis *TREM2*<sup>+</sup> TAMs promote but also the clinical value of therapeutically targeting *TREM2* to improve anti-tumor immune responses in individuals with cancer. To assess the therapeutic value of anti-*TREM2* mAb-mediated therapy, we developed a humanized anti-*TREM2* mAb, PY314, that is currently being tested clinically tested in individuals with solid tumors (ClinicalTrials.gov: NCT04691375).

## STAR★METHODS

Detailed methods are provided in the online version of this paper and include the following:

- **KEY RESOURCES TABLE**
- **RESOURCE AVAILABILITY**
  - Lead contact
  - Materials availability
  - Data and code availability
- **EXPERIMENTAL MODEL AND SUBJECT DETAILS**
  - Human tumor samples
  - Mouse strains
- **METHOD DETAILS**
  - Mouse handling and tumor implantations
  - Single cell RNA sequencing (scRNA-seq)
  - Single cell data processing
  - Cellular identification, clustering, and visualization
  - Tumor and normal tissue TREM2 expression profiling
  - Mouse tumor dissociation and flow cytometry staining
  - T cell restimulation
  - Human tumor and flow cytometry staining
  - Antibody generation
  - Mouse Fc $\gamma$ RIV (ADCC) reporter assay
  - Mouse antibody-dependent cellular phagocytosis (ADCP) assay
  - Cytokine analysis
  - FFPE tissue acquisition
  - CD8 $\alpha$  IHC staining
  - TREM2 IHC staining
  - Imaging and scoring
- **QUANTIFICATION AND STATISTICAL ANALYSIS**
- **ADDITIONAL RESOURCES**

## SUPPLEMENTAL INFORMATION

Supplemental information can be found online at <https://doi.org/10.1016/j.celrep.2021.109844>.

## ACKNOWLEDGMENTS

We thank the individuals who have enrolled in Pionyr Immunotherapeutics' clinical trials. We would also like to thank the individuals who have donated their tissues for scientific experimentation and analysis. We thank Dr. Matt Van de Rijn (Stanford University, CA) and Dr. Danielle Gibson (Histowiz Inc., NY) for assistance with evaluating and scoring the TREM2 IHC staining. Funding source: Pionyr Immunotherapeutics and its investors (<https://www.pionyrtx.com/about/#investors>).

## AUTHOR CONTRIBUTIONS

M.B., M.S., and V.S. designed the experiments. M.B., M.A., T.L., and A.C. performed the experiments unless specified otherwise. S.D. and R.P. performed *in vivo* animal experiments. J.L.P., J.R., and E.L. participated in processing and analysis of scRNA-seq data. P.C. participated in scRNA-seq encapsulations and flow cytometry processing/analysis of human tumor samples. N.S.J. and R.M. performed and managed IHC. L.L. managed protein production and purification. M.N. and S.M. performed protein production and purification. V.M.L. and X.D. performed cytokine analysis. L.R. oversaw the clinical implementation of anti-TREM2/PY314. K.P.B. oversaw the non-clinical implementation of anti-TREM2/PY314. V.J. participated in experimental conceptualization and management of experimental execution. M.F.K. conceptualized

therapeutic targeting of TREM2 on TAMs. M.B. and V.S. wrote the manuscript. M.B., M.F.K., M.S., and V.S. edited the manuscript.

## DECLARATION OF INTERESTS

M.F.K. is a founder and shareholder in Pionyr Immunotherapeutics. M.B., M.A., T.L., E.L., P.C., V.M.L., A.C., M.S., and V.S. are shareholders and former employees of Pionyr Immunotherapeutics. S.D., J.L.P., J.R., N.S.J., M.N., S.M., X.D., R.M., R.P., V.J., L.L., L.R., and K.P.B. are current employees of Pionyr Immunotherapeutics. M.S. and V.S. are inventors on US patent 10,508,148 describing anti-TREM2 antibodies. M.F.K., J.L.P., and M.B. are inventors on US patent 10,428,143 describing relevant claims.

Received: January 28, 2021

Revised: May 9, 2021

Accepted: September 27, 2021

Published: October 19, 2021

## REFERENCES

- Agata, Y., Kawasaki, A., Nishimura, H., Ishida, Y., Tsubata, T., Yagita, H., and Honjo, T. (1996). Expression of the PD-1 antigen on the surface of stimulated mouse T and B lymphocytes. *Int. Immunopharmacol.* 8, 765–772.
- Broz, M.L., Binnewies, M., Boldajipour, B., Nelson, A.E., Pollack, J.L., Erle, D.J., Barczak, A., Rosenblum, M.D., Daud, A., Barber, D.L., et al. (2014). Dissecting the tumor myeloid compartment reveals rare activating antigen-presenting cells critical for T cell immunity. *Cancer Cell* 26, 638–652.
- Butowski, N., Colman, H., De Groot, J.F., Omuro, A.M., Nayak, L., Wen, P.Y., Cloughesy, T.F., Marimuthu, A., Haidar, S., Perry, A., et al. (2016). Orally administered colony stimulating factor 1 receptor inhibitor PLX3397 in recurrent glioblastoma: an Ivy Foundation Early Phase Clinical Trials Consortium phase II study. *Neuro-oncol.* 18, 557–564.
- Calvo, E., Moreno, V., Flynn, M., Holgado, E., Olmedo, M.E., Lopez-Criado, M.P., Kahatt, C., Lopez-Vilarino, J.A., Siguero, M., Fernandez-Teruel, C., et al. (2017). Antitumor activity of lurbinectedin (PM01183) and doxorubicin in relapsed small-cell lung cancer: results from a phase I study. *Ann. Oncol.* 28, 2559–2566.
- Cassetta, L., Fragkogianni, S., Sims, A.H., Swierczak, A., Forrester, L.M., Zhang, H., Soong, D.Y.H., Cotechini, T., Anur, P., Lin, E.Y., et al. (2019). Human Tumor-Associated Macrophage and Monocyte Transcriptional Landscapes Reveal Cancer-Specific Reprogramming, Biomarkers, and Therapeutic Targets. *Cancer Cell* 35, 588–602.e10.
- Chen, L., and Flies, D.B. (2013). Molecular mechanisms of T cell co-stimulation and co-inhibition. *Nat. Rev. Immunol.* 13, 227–242.
- Cheng, S., Li, Z., Gao, R., Xing, B., Gao, Y., Yang, Y., Qin, S., Zhang, L., Ouyang, H., Du, P., et al. (2021). A pan-cancer single-cell transcriptional atlas of tumor infiltrating myeloid cells. *Cell* 184, 792–809.e23.
- Dammeijer, F., Lievense, L.A., Kaijen-Lambers, M.E., van Nimwegen, M., Bezemter, K., Hegmans, J.P., van Hall, T., Hendriks, R.W., and Aerts, J.G. (2017). Depletion of Tumor-Associated Macrophages with a CSF-1R Kinase Inhibitor Enhances Antitumor Immunity and Survival Induced by DC Immunotherapy. *Cancer Immunol. Res.* 5, 535–546.
- Dannenmann, S.R., Thielicke, J., Stöckli, M., Matter, C., von Boehmer, L., Cecconi, V., Hermanns, T., Hefermehl, L., Schraml, P., Moch, H., et al. (2013). Tumor-associated macrophages subvert T-cell function and correlate with reduced survival in clear cell renal cell carcinoma. *Oncolimmunology* 2, e23562.
- DeNardo, D.G., and Ruffell, B. (2019). Macrophages as regulators of tumour immunity and immunotherapy. *Nat. Rev. Immunol.* 19, 369–382.
- Dobin, A., Davis, C.A., Schlesinger, F., Drenkow, J., Zaleski, C., Jha, S., Batut, P., Chaisson, M., and Gingeras, T.R. (2013). STAR: ultrafast universal RNA-seq aligner. *Bioinformatics* 29 (7), 15–21.
- Efremova, M., Rieder, D., Klepsch, V., Charoentong, P., Finotello, F., Hackl, H., Hermann-Kleiter, N., Löwer, M., Baier, G., Krogsdam, A., and Trajanoski, Z.

- (2018). Targeting immune checkpoints potentiates immunoediting and changes the dynamics of tumor evolution. *Nat. Commun.* 9, 32.
- Geltink, R.I.K., Kyle, R.L., and Pearce, E.L. (2018). Unraveling the Complex Interplay Between T Cell Metabolism and Function. *Annu. Rev. Immunol.* 36, 461–488.
- Gubin, M.M., Esaulova, E., Ward, J.P., Malkova, O.N., Runci, D., Wong, P., Noguchi, T., Arthur, C.D., Meng, W., Alspach, E., et al. (2018). High-Dimensional Analysis Delineates Myeloid and Lymphoid Compartment Remodeling during Successful Immune-Checkpoint Cancer Therapy. *Cell* 175, 1014–1030.e19.
- Houde, D., Peng, Y., Berkowitz, S.A., and Engen, J.R. (2010). Post-translational modifications differentially affect IgG1 conformation and receptor binding. *Mol. Cell. Proteomics* 9, 1716–1728.
- Jahchan, N.S., Mujal, A.M., Pollack, J.L., Binnewies, M., Sriram, V., Reyno, L., and Krummel, M.F. (2019). Tuning the Tumor Myeloid Microenvironment to Fight Cancer. *Front. Immunol.* 10, 1611.
- Jenkins, R.W., Barbie, D.A., and Flaherty, K.T. (2018). Mechanisms of resistance to immune checkpoint inhibitors. *Br. J. Cancer* 118, 9–16.
- Kaneda, M.M., Cappello, P., Nguyen, A.V., Ralainirina, N., Hardamon, C.R., Foubert, P., Schmid, M.C., Sun, P., Mose, E., Bouvet, M., et al. (2016). Macrophage PI3K $\gamma$  Drives Pancreatic Ductal Adenocarcinoma Progression. *Cancer Discov.* 6, 870–885.
- Katzenellenbogen, Y., Sheban, F., Yalin, A., Yofe, I., Svetlichny, D., Jaitin, D.A., Bornstein, C., Moshe, A., Keren-Shaul, H., Cohen, M., et al. (2020). Coupled scRNA-Seq and Intracellular Protein Activity Reveal an Immunosuppressive Role of TREM2 in Cancer. *Cell* 182, 872–885.e19.
- Komohara, Y., Jinushi, M., and Takeya, M. (2014). Clinical significance of macrophage heterogeneity in human malignant tumors. *Cancer Sci.* 105, 1–8.
- Lau, J., Cheung, J., Navarro, A., Lianoglou, S., Haley, B., Totpal, K., Sanders, L., Koeppen, H., Caplazi, P., McBride, J., et al. (2017). Tumour and host cell PD-L1 is required to mediate suppression of anti-tumour immunity in mice. *Nat. Commun.* 8, 14572.
- Lavin, Y., Kobayashi, S., Leader, A., Amir, E.D., Elefant, N., Bigenwald, C., Remark, R., Sweeney, R., Becker, C.D., Levine, J.H., et al. (2017). Innate Immune Landscape in Early Lung Adenocarcinoma by Paired Single-Cell Analyses. *Cell* 169, 750–765.e17.
- Le, D.T., Durham, J.N., Smith, K.N., Wang, H., Bartlett, B.R., Aulakh, L.K., Lu, S., Kemberling, H., Wilt, C., Luber, B.S., et al. (2017). Mismatch repair deficiency predicts response of solid tumors to PD-1 blockade. *Science* 357, 409–413.
- Lewis, C.E., and Pollard, J.W. (2006). Distinct role of macrophages in different tumor microenvironments. *Cancer Res.* 66, 605–612.
- Lin, E.Y., and Pollard, J.W. (2007). Tumor-associated macrophages press the angiogenic switch in breast cancer. *Cancer Res.* 67, 5064–5066.
- Matulonis, U.A., Shapira-Frommer, R., Santin, A.D., Lisyanskaia, A.S., Pignata, S., Vergote, I., Raspagliesi, F., Sonke, G.S., Birrer, M., Provencher, D.M., et al. (2019). Antitumor activity and safety of pembrolizumab in patients with advanced recurrent ovarian cancer: results from the phase II KEYNOTE-100 study. *Ann. Oncol.* 30, 1080–1087.
- Miller, B.C., Sen, D.R., Al Abosy, R., Bi, K., Virkud, Y.V., LaFleur, M.W., Yates, K.B., Lako, A., Felt, K., Naik, G.S., et al. (2019). Subsets of exhausted CD8 $^{+}$  T cells differentially mediate tumor control and respond to checkpoint blockade. *Nat. Immunol.* 20, 326–336.
- Molgora, M., Esaulova, E., Vermi, W., Hou, J., Chen, Y., Luo, J., Brioschi, S., Bugatti, M., Omodei, A.S., Ricci, B., et al. (2020). TREM2 Modulation Remodels the Tumor Myeloid Landscape Enhancing Anti-PD-1 Immunotherapy. *Cell* 182, 886–900.e17.
- Nywening, T.M., Wang-Gillam, A., Sanford, D.E., Belt, B.A., Panni, R.Z., Cusworth, B.M., Toriola, A.T., Nieman, R.K., Worley, L.A., Yano, M., et al. (2016). Targeting tumour-associated macrophages with CCR2 inhibition in combination with FOLFIRINOX in patients with borderline resectable and locally advanced pancreatic cancer: a single-centre, open-label, dose-finding, non-randomised, phase 1b trial. *Lancet Oncol.* 17, 651–662.
- Obradovic, A., Chowdhury, N., Haake, S.M., Ager, C., Wang, V., Vlahos, L., Guo, X.V., Aggen, D.H., Rathmell, W.K., Jonasch, E., et al. (2021). Single-cell protein activity analysis identifies recurrence-associated renal tumor macrophages. *Cell* 184, 2988–3005.e16.
- Pauken, K.E., Sammons, M.A., Odorizzi, P.M., Manne, S., Godec, J., Khan, O., Drake, A.M., Chen, Z., Sen, D.R., Kurachi, M., et al. (2016). Epigenetic stability of exhausted T cells limits durability of reinvigoration by PD-1 blockade. *Science* 354, 1160–1165.
- Penny, H.L., Sieow, J.L., Adriani, G., Yeap, W.H., See Chi Ee, P., San Luis, B., Lee, B., Lee, T., Mak, S.Y., Ho, Y.S., et al. (2016). Warburg metabolism in tumor-conditioned macrophages promotes metastasis in human pancreatic ductal adenocarcinoma. *Oncolimmunology* 5, e1191731.
- Peranzoni, E., Lemoine, J., Vimeux, L., Feuillet, V., Barrin, S., Kantari-Mimoun, C., Bercovici, N., Guérin, M., Biton, J., Ouakrim, H., et al. (2018). Macrophages impede CD8 T cells from reaching tumor cells and limit the efficacy of anti-PD-1 treatment. *Proc. Natl. Acad. Sci. USA* 115, E4041–E4050.
- Philip, M., Fairchild, L., Sun, L., Horste, E.L., Camara, S., Shakiba, M., Scott, A.C., Viale, A., Lauer, P., Merghoub, T., et al. (2017). Chromatin states define tumour-specific T cell dysfunction and reprogramming. *Nature* 545, 452–456.
- Puig-Kröger, A., Sierra-Filardi, E., Domínguez-Soto, A., Samaniego, R., Corcuera, M.T., Gómez-Aguado, F., Ratnam, M., Sánchez-Mateos, P., and Corbí, A.L. (2009). Folate receptor beta is expressed by tumor-associated macrophages and constitutes a marker for M2 anti-inflammatory/regulatory macrophages. *Cancer Res.* 69, 9395–9403.
- Qian, B., Deng, Y., Im, J.H., Muschel, R.J., Zou, Y., Li, J., Lang, R.A., and Pollard, J.W. (2009). A distinct macrophage population mediates metastatic breast cancer cell extravasation, establishment and growth. *PLoS ONE* 4, e6562.
- Ruffell, B., Chang-Strachan, D., Chan, V., Rosenbusch, A., Ho, C.M., Pryer, N., Daniel, D., Hwang, E.S., Rugo, H.S., and Coussens, L.M. (2014). Macrophage IL-10 blocks CD8 $^{+}$  T cell-dependent responses to chemotherapy by suppressing IL-12 expression in intratumoral dendritic cells. *Cancer Cell* 26, 623–637.
- Satija, R, Farrell, R.A., Gennert, D, Schier, A.F., and Regev, A (2015). Spatial reconstruction of single-cell gene expression data. *Nature biotechnology* 33 (5), 495–502. <https://doi.org/10.1038/nbt.3192>.
- Shields, R.L., Lai, J., Keck, R., O'Connell, L.Y., Hong, K., Meng, Y.G., Weikert, S.H., and Presta, L.G. (2002). Lack of fucose on human IgG1 N-linked oligosaccharide improves binding to human Fcgamma RIII and antibody-dependent cellular toxicity. *J. Biol. Chem.* 277, 26733–26740. <https://doi.org/10.1074/jbc.M202069200>.
- Stuart, T., Butler, A., Hoffman, P., Hafemeister, C., Papalexi, E., Mauck, W.M., 3rd, Hao, Y., Stoeckius, M., Smibert, P., and Satija, R. (2019). Comprehensive Integration of Single-Cell Data. *Cell* 177, 1888–1902.e21.
- Takahashi, K., Rochford, C.D., and Neumann, H. (2005). Clearance of apoptotic neurons without inflammation by microglial triggering receptor expressed on myeloid cells-2. *J. Exp. Med.* 201, 647–657.
- Tang, Z., Kang, B., Li, C., Chen, T., and Zhang, Z. (2019). GEPIA2: an enhanced web server for large-scale expression profiling and interactive analysis. *Nucleic acids research* 47 (W1), W556–W560. <https://doi.org/10.1093/nar/gkz430>.
- Tothill, R.W., Tinker, A.V., George, J., Brown, R., Fox, S.B., Lade, S., Johnson, D.S., Trivett, M.K., Etemadmoghadam, D., Locandro, B., et al.; Australian Ovarian Cancer Study Group (2008). Novel molecular subtypes of serous and endometrioid ovarian cancer linked to clinical outcome. *Clin. Cancer Res.* 14, 5198–5208.
- Trapnell, C., Cacchiarelli, D., Grimsby, J., Pokharel, P., Li, S., Morse, M., Lennon, N.J., Livak, K.J., Mikkelsen, T.S., and Rinn, J.L. (2014). The dynamics and regulators of cell fate decisions are revealed by pseudotemporal ordering of single cells. *Nat. Biotechnol.* 32, 381–386.
- Viitala, M., Virtakoivu, R., Tadayon, S., Rannikko, J., Jalkanen, S., and Hollmén, M. (2019). Immunotherapeutic Blockade of Macrophage Clever-1

- Reactivates the CD8<sup>+</sup> T-cell Response against Immunosuppressive Tumors. *Clin. Cancer Res.* 25, 3289–3303.
- Walunas, T.L., Lenschow, D.J., Bakker, C.Y., Linsley, P.S., Freeman, G.J., Green, J.M., Thompson, C.B., and Bluestone, J.A. (1994). CTLA-4 can function as a negative regulator of T cell activation. *Immunity* 1, 405–413.
- Wang, T., Xiao, M., Ge, Y., Krepler, C., Belser, E., Lopez-Coral, A., Xu, X., Zhang, G., Azuma, R., Liu, Q., et al. (2015). BRAF Inhibition Stimulates Melanoma-Associated Macrophages to Drive Tumor Growth. *Clin. Cancer Res.* 21, 1652–1664.
- Wilky, B.A. (2019). Immune checkpoint inhibitors: The linchpins of modern immunotherapy. *Immunol. Rev.* 290, 6–23.
- Xiong, H., Mittman, S., Rodriguez, R., Moskalenko, M., Pacheco-Sanchez, P., Yang, Y., Nickles, D., and Cubas, R. (2019). Anti-PD-L1 Treatment Results in Functional Remodeling of the Macrophage Compartment. *Cancer Res.* 79, 1493–1506.
- Yamane-Ohnuki, N., and Satoh, M. (2009). Production of therapeutic antibodies with controlled fucosylation. *MAbs* 1, 230–236.
- Zhang, Q.W., Liu, L., Gong, C.Y., Shi, H.S., Zeng, Y.H., Wang, X.Z., Zhao, Y.W., and Wei, Y.Q. (2012). Prognostic significance of tumor-associated macrophages in solid tumor: a meta-analysis of the literature. *PLoS ONE* 7, e50946.

## STAR★METHODS

### KEY RESOURCES TABLE

REAGENT or RESOURCE	SOURCE	IDENTIFIER
<b>Antibodies</b>		
anti-mouse XCR1 BV421 (clone ZET)	Biolegend	Cat # 148216; AB_2565230
anti-mouse F4/80 biotin (clone BM8)	Biolegend	Cat # 123106; AB_893501
Streptavidin BV510	Biolegend	Cat # 405234
anti-mouse CD64 BV605 (clone X54-5/7.1)	Biolegend	Cat # 139323; AB_2629778
anti-mouse CD11c BV650 (clone N418)	Biolegend	Cat # 117339; AB_2562414
anti-mouse Ly-6C BV711 (clone HK1.4)	Biolegend	Cat # 128037; AB_2562630
anti-mouse CD90.2 BV785 (clone 30-H12)	Biolegend	Cat # 105331; AB_2562900
anti-mouse NKp46 BV785 (clone 29A1.4)	Biolegend	Cat # 137637; AB_2734201
anti-mouse/human CD45R/B220 BV785 (clone RA3-6B2)	Biolegend	Cat # 103246; AB_2563256
anti-mouse/human CD11b AF488 (clone M1/70)	Biolegend	Cat # 101217; AB_389305
anti-mouse CD45 PerCP/Cy5.5 (clone 30-F11)	Biolegend	Cat # 103132; AB_893340
anti-mouse Ly6G PE-e610 (clone 1A8-Ly6g)	Invitrogen	Cat # 61-9668-82; AB_2574679
anti-mouse CD24 PE/Cy7 (clone M1/69)	Biolegend	Cat # 101822; AB_756048
anti-mouse MHC-II AF700 (clone M5/114.15.2)	Biolegend	Cat # 107622; AB_493727
anti-mouse CD40 PE (clone 3/23)	Biolegend	Cat # 124610; AB_1134075
anti-mouse CD86 PE (clone GL-1)	Biolegend	Cat # 105008; AB_313151
Rat IgG2a, κ PE isotype control PE (clone RTK2758)	Biolegend	Cat # 400508; AB_326530
anti-mouse/human TREM2 APC (clone 237920)	R&D Systems	Cat # FAB17291A; AB_884527
Rat IgG2b APC (clone 141945)	R&D Systems	Cat # IC013A; AB_357257
anti-mouse/human CD45R BV605 (clone RA3-6B2)	Biolegend	Cat # 103244; AB_2563312
anti-mouse NKp46 BV650 (clone clone 29A1.4)	Biolegend	Cat # 137635; AB_2734200
anti-mouse/human CD44 BV711 (clone IM7)	Biolegend	Cat # 103057; AB_2564214
anti-mouse CD279/PD-1 FITC (clone RMP1-30)	Invitrogen	Cat # 11-9981-82; AB_2564214
anti-mouse CD8a PerCP/Cy5.5 (clone 53-6.7)	Biolegend	Cat # 100734; AB_2075238
anti-mouse/human TOX PE (clone REA473)	Miltenyi Biotec	Cat # 130-120-716; AB_2801780
anti-mouse/human CD11b PE-e610 (clone M1/70)	Invitrogen	Cat # 61-0112-82; AB_2574528
anti-mouse CD4 PE/Cy7 (clone GK1.5)	Biolegend	Cat # 100422; AB_312707
anti-mouse FOXP3 A647 (clone MF-14)	Biolegend	Cat # 126408; AB_1089115
anti-mouse CD45 A700 (clone 30-F11)	Biolegend	Cat # 103128; AB_493715
anti-mouse TNF-α BV421 (clone MP6-XT22)	Biolegend	Cat # 506328; AB_2562902
anti-mouse IFNg BV605 (clone XMG1.2)	Biolegend	Cat # 505839; AB_2561438
anti-human CD45 PE (cone H130)	Biolegend	Cat # 304058; AB_2564156

(Continued on next page)

**Continued**

REAGENT or RESOURCE	SOURCE	IDENTIFIER
anti-human CD274 (PD-L1) BV421 (clone MIH1)	BD Biosciences	Cat # 563738; AB_2738396
anti-human CD16 BV605 (clone 3G8)	Biolegend	Cat # 302040; AB_2562990
anti-human CD15 BV650 (clone HI98)	BD Biosciences	Cat # 564232; AB_2738686
anti-human CD14 BV711 (clone M5E2)	Biolegend	Cat # 301838; AB_2562909
anti-human CD56 BV785 (clone B159)	Biolegend	Cat # 362550; AB_2566059
anti-human CD3 BV785 (clone OKT3)	Biolegend	Cat # 317330; AB_2563507
anti-human CD20 BV785 (clone 2H7)	Biolegend	Cat # 302356; AB_2566316
anti-human CD19 BV785 (clone HIB19)	Biolegend	Cat # 302240; AB_2563442
anti-human APOE AF488 (clone EP1374Y)	Abcam	Cat # ab196463
anti-human CD89 BB700 (clone A59)	BD Biosciences	Cat # 746042; AB_2743427
anti-human CD88 PE/Dazzle594 (clone S5/1)	Biolegend	Cat # 344318; AB_2750447
anti-human CD123 PerCP/Cy5 (clone 6H6)	Fisher	Cat # 50-158-17; AB_10718981
anti-human BDCA-1 PE/Cy7 (clone L161)	Biolegend	Cat # 331516; AB_2275574
anti-human CD11c APC/R700 (clone 3.9)	BD Biosciences	Cat # 566610; AB_2869792
anti-human BDCA-3 APC/Vio770 (clone AD5-14H12)	Miltenyi Biotec	Cat # 130-113-315; AB_2726092
anti-human HLA-DR BUV395 (clone G46-6)	BD Biosciences	Cat # 564040; AB_2738558
anti-human CD45 BUV496 (clone HI30)	BD Biosciences	Cat # 750179; AB_2868405
anti-human CD64 BUV737 (clone 10.1)	BD Biosciences	Cat # 612776; AB_2870105
<b>Biological samples</b>		
DTC (Flow), Patient ID# 110003338 Breast Cancer, Invasive/Infiltrating Ductal	Discovery Life Sciences	Cat # BTC1000-K9110003338112817MS
DTC (Flow), Patient ID# 110037013 Breast Cancer	Discovery Life Sciences	Cat # BTC1000-G2110037013040418MS
DTC (Flow), Patient ID# 110045042 Ovarian Cancer, Carcinosarcoma (MMMT)	Discovery Life Sciences	Cat # BTC1000-N1110045042040119MS
DTC (Flow), Patient ID# 110045087 Kidney Cancer, Renal Cell Carcinoma	Discovery Life Sciences	Cat # BTC1000-N1110045087071019MS
DTC (Flow), Patient ID# 121284861 Kidney Cancer, Renal Cell Carcinoma	Discovery Life Sciences	Cat # BTC1000-K3121284861022619MS
DTC (Flow), Patient ID# 121284920 Kidney Cancer, Clear Cell Renal Cell	Discovery Life Sciences	Cat # BTC1000-G9121284920022819MS
DTC (Flow), Patient ID# 121330637 Head and Neck Cancer, Squamous Cell	Discovery Life Sciences	Cat # BTC1000-K3121330637041619MS
DTC (Flow), Patient ID# 121392108 Head and Neck Cancer, Squamous Cell	Discovery Life Sciences	Cat # BTC1000-J9121392108062719MS
DTC (Flow), Patient ID# 200000163 Breast Cancer	Discovery Life Sciences	Cat # BTC1000-G2200000163050819MS
DTC (Flow), Patient ID# 200000245 Breast Cancer, Invasive/Infiltrating Ductal	Discovery Life Sciences	Cat # BTC1000-E1200000245041719MS
DTC (Flow), Patient ID# 200000666 Head and Neck Cancer, Squamous Cell	Discovery Life Sciences	Cat # BTC1000-G2200000666081919MS
DTC (Flow), Patient ID# 200000744 Ovarian Cancer, Endometrioid Tumors	Discovery Life Sciences	Cat # BTC1000-G2200000744090219MS
DTC (Flow), Patient ID# 200000891 Head and Neck Cancer, Squamous Cell	Discovery Life Sciences	Cat # BTC1000-G2200000891110519MS
DTC (Flow), Patient ID# 200000955 Ovarian Cancer, Undefined	Discovery Life Sciences	Cat # BTC1000-E1200000955093019MS
DTC (Flow), Patient ID# 200000966 Ovarian Cancer, Serous Carcinoma	Discovery Life Sciences	Cat # BTC1000-E1200000966091719MS

(Continued on next page)

**Continued**

REAGENT or RESOURCE	SOURCE	IDENTIFIER
DTC (Flow), Patient ID# 200001057 Kidney Cancer, Clear Cell	Discovery Life Sciences	Cat # BTC1000-G2200001057040219MS
DTC (Flow), Patient ID# 200002408 Kidney Cancer, Clear Cell	Discovery Life Sciences	Cat # BTC1000-E1200002408091319MS
DTC (Flow), Patient ID# 200002423 Kidney Cancer, Clear Cell Renal Cell	Discovery Life Sciences	Cat # BTC1000-1C200002423091119MS
DTC (Flow), Patient ID# 200002445 Ovarian Cancer, Undefined	Discovery Life Sciences	Cat # BTC1000-E1200002445092519MS
DTC (Flow), Patient ID# 200004205 Head and Neck Cancer, Squamous Cell	Discovery Life Sciences	Cat # BTC1000-G2200004205102819MS
DTC (Flow), Patient ID# 200005048 Head and Neck Cancer, Squamous Cell	Discovery Life Sciences	Cat # BTC1000-G2200005048052019MS
DTC (Flow), Patient ID# 200011123 Ovarian Cancer, Carcinosarcoma (MMMT)	Discovery Life Sciences	Cat # BTC1000-E1200011123090219MS
DTC (Flow), Patient ID# 110006760 Bladder Cancer, Transitional Cell Carcinoma (Papillary)	Discovery Life Sciences	Cat # BTC1000-E1110006760080618MS
DTC (Flow), Patient ID# 110039923 Bladder Cancer, Transitional Cell Carcinoma NOS	Discovery Life Sciences	Cat # BTC1000-G2110039923082818MS
DTC (Flow), Patient ID# 110043228 Prostate Cancer, Adenocarcinoma	Discovery Life Sciences	Cat # BTC1000-G2110043228120418MS
DTC (Flow), Patient ID# 110045001 Endometrial Cancer, Adenocarcinoma	Discovery Life Sciences	Cat # BTC1000-N1110045001010919MS
DTC (Flow), Patient ID# 110047059 Breast Cancer, Invasive Ductal Carcinoma	Discovery Life Sciences	Cat # BTC1000-G0110047059102819MS
DTC (Flow), Patient ID# 121465459 Prostate Cancer, Adenocarcinoma	Discovery Life Sciences	Cat # BTC1000-K5121465459091719MS
DTC (Flow), Patient ID# 200000025 Endometrial Cancer, Adenocarcinoma	Discovery Life Sciences	Cat # BTC1000-G220000025073019MS
DTC (Flow), Patient ID# 200000637 Endometrial Cancer, Adenocarcinoma	Discovery Life Sciences	Cat # BTC1000-G2200000637090919MS
DTC (Flow), Patient ID# 200000701 Bladder Cancer, Transitional Cell Carcinoma	Discovery Life Sciences	Cat # BTC1000-G2200000701082019MS
DTC (Flow), Patient ID# 200000746 Prostate Cancer	Discovery Life Sciences	Cat # BTC1000-G2200000746092319MS
DTC (Flow), Patient ID# 200000775 Breast Cancer, Invasive Mammary Carcinoma	Discovery Life Sciences	Cat # BTC1000-E1200000775082019MS
DTC (Flow), Patient ID# 200000867 Prostate Cancer, Adenocarcinoma	Discovery Life Sciences	Cat # BTC1000-G2200000867091819MS
DTC (Flow), Patient ID# 200000967 Endometrial Cancer, Undefined	Discovery Life Sciences	Cat # BTC1000-E1200000967091819MS
DTC (Flow), Patient ID# 200002595 Breast Cancer, Invasive Ductal Carcinoma	Discovery Life Sciences	Cat # BTC1000-3C200002595012020MS
DTC (Flow), Patient ID# 200003133 Bladder Cancer, Transitional Cell Carcinoma	Discovery Life Sciences	Cat # BTC1000-G2200003133030419MS
DTC (Flow), Patient ID# 200003427 Endometrial Cancer, Adenocarcinoma	Discovery Life Sciences	Cat # BTC1000-G2200003427040919MS
DTC (Flow), Patient ID# 200003916 Bladder Cancer	Discovery Life Sciences	Cat # BTC1000-E1200003916090219MS
DTC (Flow), Patient ID# 200003918 Endometrial Cancer, Adenocarcinoma	Discovery Life Sciences	Cat # BTC1000-E1200003918081419MS
DTC (Flow), Patient ID# 200005300 Bladder Cancer, Transitional Cell Carcinoma (Papillary)	Discovery Life Sciences	Cat # BTC1000-E1200005300062619MS

(Continued on next page)

**Continued**

REAGENT or RESOURCE	SOURCE	IDENTIFIER
DTC (Flow), Patient ID# 200005541 Prostate Cancer	Discovery Life Sciences	Cat # BTC1000-E1200005541082619MS
DTC (Flow), Patient ID# 200005514 Ovarian Cancer, Serous Carcinoma	Discovery Life Sciences	Cat # BTC1000-E1200005514080619MS
DTC (Flow), Patient ID# 200000118 Colorectal Cancer, Adenocarcinoma	Discovery Life Sciences	Cat # BTC1000-G220000118032719MS
DTC (Flow), Patient ID# 110042159 Colorectal Cancer, Adenocarcinoma	Discovery Life Sciences	Cat # BTC1000-G2110042159042018MS
DTC (Flow), Patient ID# 110043544 Ovarian Cancer, Serous Carcinoma	Discovery Life Sciences	Cat # BTC1000-G0110043544012120MS
DTC (Flow), Patient ID# 200011104 Colorectal Cancer, Adenocarcinoma	Discovery Life Sciences	Cat # BTC1000-E1200011104081619MS
DTC (Flow), Patient ID# 110045042 Ovarian Cancer	Discovery Life Sciences	Cat # BTC1000-N1110045042040119MS
DTC (Flow), Patient ID# 200003071 Colorectal Cancer, Adenocarcinoma	Discovery Life Sciences	Cat # BTC1000-G2200003071071919MS
DTC (scRNA-Seq), Patient ID# 110045042 Ovarian Cancer	Discovery Life Sciences	Cat # BTC1000-N1110045042040119MS
DTC (scRNA-Seq), Patient ID# 110042463 Bladder Cancer, Transitional Cell Carcinoma NOS	Discovery Life Sciences	Cat # BTC1000-E1110042463022619MS
DTC (scRNA-Seq), Patient ID# 121276262 Endometrial Cancer, Serous Carcinoma	Discovery Life Sciences	Cat # BTC1000-J9121276262022019MS
DTC (scRNA-Seq), Patient ID# 110005709 Gastric Cancer, Adenocarcinoma	Discovery Life Sciences	Cat # BTC1000-J7110005709101717MS
DTC (scRNA-Seq), Patient ID# 121362435 Kidney Cancer, Renal Cell Carcinoma	Discovery Life Sciences	Cat # BTC1000-G9121362435052019MS
DTC (scRNA-Seq), Patient ID# 200001077 Breast Cancer	Discovery Life Sciences	Cat # BTC1000-G2200001077050319MS
DTC (scRNA-Seq), Patient ID# 200005529 Colorectal Cancer	Discovery Life Sciences	Cat # BTC1000-E1200005529071519MS
DTC (scRNA-Seq), Patient ID# 200003216 Head and Neck Cancer, Squamous Cell	Discovery Life Sciences	Cat # BTC1000-G2200003216050719MS
DTC (scRNA-Seq), Patient ID# 110045033 Ovarian Cancer, Serous Carcinoma	Discovery Life Sciences	Cat # BTC1000-N1110045033031419MS
DTC (scRNA-Seq), Patient ID# 200001001 Lung Cancer, Squamous Cell Carcinoma	Discovery Life Sciences	Cat # BTC1000-G2200001001021819MS
Human Ovarian Tissue Microarray (42 patients)	Reveal Biosciences	N/A
Mouse Tumor Tissue	Pionyr Immunotherapeutics	N/A
<b>Chemicals, peptides, and recombinant proteins</b>		
Tumor Dissociation Kit, mouse	Miltenyi Biotec	Cat # 130-096-730
Tumor Dissociation Kit, human	Miltenyi Biotec	Cat # 130-095-929
Halt Protease Inhibitor Cocktail (100X)	Thermo Scientific	Cat # 78429
Phorbol 12-myristate 13-acetate (PMA)	Sigma-Aldrich	Cat # P8139
Ionomycin	Invitrogen	Cat # I24222
Monensin Solution (1000X)	Thermo Fisher	Cat # 00-4505-51
Brefeldin A (BFA)	Sigma-Aldrich	Cat # B7651
16% Paraformaldehyde Aqueous Solution	Electron Microscopy Sciences	Cat # 15710
Recombinant Murine IFN- $\gamma$	Peptech	Cat # 315-05
LPS-EB	Invivogen	Cat # tirl-eblps
DAPI Solution (1 mg/mL)	Thermo Scientific	Cat # 62248

(Continued on next page)

**Continued**

REAGENT or RESOURCE	SOURCE	IDENTIFIER
CellTrace Violet Cell Proliferation Kit	Invitrogen	Cat # C34557
Zombie NIR Fixable Viability Kit	Biolegend	Cat # 423106
LIVE/DEAD Fixable Aqua Dead Cell Stain Kit	Invitrogen	Cat # L34957
Fc Receptor Blocker	Innovex Biosciences	Cat # 007-000-001
Brilliant Stain Buffer Plus	BD Biosciences	Cat # 566385
RPMI-1640	GIBCO	Cat # 11220035
Waymouth's	GIBCO	Cat # 11220035
Iscove's Modified Dulbecco's Medium (IMDM)	GIBCO	Cat # 12440053
DPBS, no calcium, no magnesium	GIBCO	Cat # 14190144
Bovine Serum Albumin solution (30% in DPBS)	Sigma-Aldrich	Cat # A9576-50ML
UltraPure 0.5M EDTA, pH 8.0	Invitrogen	Cat # 15575020
Hyclone Super Low IgG Fetal Bovine Serum	GE Healthcare Life Sciences	Cat # SH30898.03
2-Mercaptoethanol	GIBCO	Cat # 21985023
Antibiotic-Antimycotic (100X)	GIBCO	Cat # 15240062
<b>Critical commercial assays</b>		
Chromium Single Cell 30 Library & Gel Bead Kit V3	10X Genomics	Cat # 1000075
Mouse Fc $\gamma$ RIV ADCC Bioassay	Promega	Cat # M1201
V-PLEX Mouse Cytokine 19-Plex Kit	MSD	Cat # K15255D
Foxp3 / Transcription Factor Staining Buffer Set	Invitrogen	Cat # 00-5523-00
<b>Deposited data</b>		
Single cell RNA sequencing data (mouse and human)	This paper	GEO: GSE165404
Original code	This paper	Zenodo: <a href="https://zenodo.org/record/5366120">https://zenodo.org/record/5366120</a>
<b>Experimental models: Cell lines</b>		
CT26.WT	ATCC	Cat # CRL-2638; CVCL_7256
EMT6	ATCC	Cat # CRL-2755; CVCL_1923
HEK293	ATCC	Cat # CRL-1573; CVCL_0045
<b>Experimental models: Organisms/strains</b>		
C57BL/6 (C57BL/6J)	The Jackson Laboratory	Cat # 000664; IMSR_JAX:000664
BALB/c	Taconic	Cat # BALB/cAnNTac; IMSR_TAC:balb
B6 Albino (C57BL/6NTac-Tyrtm1Arte)	Taconic	Cat # C57BL/6NTac-Tyrtm1Arte; IMSR_TAC:11971
<b>Software and algorithms</b>		
10X Genomics Cell Ranger v3.0.2	10X Genomics	<a href="https://www.10xgenomics.com">https://www.10xgenomics.com</a>
STAR	(Dobin et al., 2013)	<a href="https://code.google.com/archive/p/rna-star">https://code.google.com/archive/p/rna-star</a>
Seurat	(Satija et al., 2015)	<a href="https://satijalab.org/seurat/">https://satijalab.org/seurat/</a>
R: The Project for Statistical Computing	N/A	<a href="http://www.r-project.org/">http://www.r-project.org/</a>
<b>Other</b>		
Graphical abstract	BioRender	<a href="http://biorender.com">biorender.com</a>

## RESOURCE AVAILABILITY

### Lead contact

Further information and requests for resources and reagents should be directed to and will be fulfilled, when possible, by Kevin P. Baker ([kbaker@pionyrtx.com](mailto:kbaker@pionyrtx.com)).

### Materials availability

Reagents used in this study can be made available following completion of a Materials Transfer Agreement.

### Data and code availability

- Single-cell RNA-seq data have been deposited at the Gene Expression Omnibus (GEO) and are publicly available as of the date of publication. Accession numbers are listed in the [Key resources table](#).
- All original code has been deposited at Zenodo and is publicly available as of the date of publication. DOIs are listed in the [Key resources table](#).
- Any additional information required to reanalyze the data reported in this paper is available from the Lead Contact upon reasonable request.

## EXPERIMENTAL MODEL AND SUBJECT DETAILS

### Human tumor samples

Human tumor samples used for both flow cytometry and single-cell RNA sequencing were acquired from Discovery Life Sciences. 49 human tumor samples were used for flow cytometric analysis of immune composition and TREM2 surface levels. 10 human tumor samples were used for single-cell RNA sequencing. Clinicopathological details are provided in [Table S2](#). Neither age, gender, nor race were factored into selection of human tumor samples.

### Mouse strains

Studies involving mice were approved by either the Murigenics Animal Studies Committee, the Explora Biolabs Institutional Animal Care and Use Committee, or the Stony Brook University Institutional Animal Care and Use Committee. For studies performed at Pionyrt Immunotherapeutics (CT26 and EMT6 studies), female C57BL/6 and BALB/c mice (6–8 weeks old) were purchased from Taconic or The Jackson Laboratory and used after one week of acclimatization at the animal facility.

## METHOD DETAILS

### Mouse handling and tumor implantations

Subconfluent tumor cells were harvested within 4 to 8 subcultures after thaw from liquid nitrogen stock and then used for the *in vivo* experiments. The right ventro-lateral area of female mice was shaved and prepared for injection a day in advance of tumor cell inoculation. On the day of tumor inoculation, the cells were harvested and used within 30 minutes. To establish subcutaneous tumors,  $0.5 \times 10^6$  EMT6 cells or  $1 \times 10^6$  CT26 cells were implanted subcutaneously. Tumor volume growth was monitored via perpendicular tumor diameter measurements and calculated using the formula: tumor volume ( $\text{mm}^3$ ) =  $0.5 \times (\text{length}) \times (\text{width})^2$ . For drug treatments, mice were dosed intraperitoneally every 5 days with indicated antibodies once the tumor volume of the implanted cohort reached required tumor volume. The animals were allowed *ad libitum* access to Lab Diet rodent chow and water. Mice were monitored a minimum of twice per week by the investigator or veterinary staff for clinical abnormalities which may require euthanasia. Mice were euthanized when they showed a net body weight loss > 20% compared to baseline weight measurement or when the tumor volumes reached  $\sim 2000 \text{ mm}^3$ .

ID8<sup>Luc2</sup> studies were performed at AJES Life Sciences (now L2P Research). Briefly, 10–12 week old female C57BL/6NTac-Tyr<sup>tm1Arte</sup> were purchased from Taconic and acclimated for 1 week prior to initiation of study. ID8<sup>Luc2</sup> cells were cultured and harvested in a similar manner to the above methods. To establish intraperitoneal tumors,  $5 \times 10^6$  ID8<sup>Luc2</sup> cells were injected by intraperitoneal injection. When the absolute luminescence (photons/sec/cm<sup>2</sup>/s) measured through optimal imaging reached an average of 40,000–50,000, mice were randomized and dosed with antibody. Luminescence was measured approximately once per week per animal.

### Single cell RNA sequencing (scRNA-seq)

For mouse scRNA-seq, CT26 tumors were dissociated and processed as indicated above. For the untreated mouse CT26 tumors, 5 tumors were pooled. For comparison of post-treatment CT26 samples, the 3 tumors closest to the median tumor size within each treatment condition were pooled. For each sample pool, live (DAPI<sup>-</sup>) CD45<sup>+</sup> cells were sorted on a BD FACSaria Fusion. For the human samples, 1 mL of frozen, dissociated tumor cells were purchased from Discovery Life Sciences. The frozen pellet was thawed in a 37°C water bath and gradually diluted with 25 mL of warm RPMI containing 10% FBS and 10mM HEPES, and centrifuged for 5 min at 550 rcf. The cell pellet was stained with anti-CD45-PE (clone HI30, Biolegend). DAPI<sup>-</sup>, CD45<sup>+</sup> cells were sorted on a BD FACSaria

Fusion. After sorting, cells were washed with 3 mL of 0.04% BSA/PBS three times and resuspended at  $5 \times 10^5$  cells/mL. The cells were loaded into a Chromium Chip B for a targeted cell encapsulation of 10,000 cells, and placed into the Chromium Controller (10X Genomics, Single Cell 3' v3 Reagent Kit). Post GEM-RT cleanup, cDNA amplification, and library construction was performed according to the Single Cell 3' v3 user manual from 10X Genomics. The libraries were sequenced on a NovaSeq by MedGenome Inc. Samples from the post-treatment CT26 experiment were all processed simultaneously on the same chip and libraries were prepared at the same time in order to avoid batch effects.

### Single cell data processing

Sequencing data was processed using 10X Genomics Cell Ranger v3.0.2 pipeline. MedGenome Inc. provided fastq files for each sample by converting raw, Illumina bcl files into fastq files using the Cell Ranger subroutine *mkfastq*. Afterward, Cell Ranger *count* was run, which utilizes STAR (Dobin et al., 2013) to align reads against the reference genomes mm10 or GRCh38 for mouse or human cells, respectively. After filtering reads with redundant unique molecular identifiers (UMI), *count* generated gene-cellular barcode files (filtered\_feature\_bc\_matrix folder consisting of barcodes.tsv, features.tsv, and matrix mtx). Both *mkfastq* and *count* were run with default parameters.

### Cellular identification, clustering, and visualization

For each sample, the filtered\_feature\_bc\_matrix files were passed to the R (v. 3.6.0) software package Seurat (Satija et al., 2015) (<http://satijalab.org/seurat/>) (v2.3.4) for all downstream analyses. The features.tsv file was renamed to genes.tsv to be compatible with the *Read10X* function. We then filtered on cells that expressed a minimum of 200 genes and required that all genes be expressed in at least 3 cells and have not more than 8500 UMI. We also removed cells that contained > 20% of reads associated with mitochondria genes and > 45% of reads associated with ribosomal genes. Count data was then log transformed and scaled using each remaining cell's UMI count and proportion of mitochondrial and ribosomal genes as nuisance factors (implemented in Seurat's *ScaleData* function) to correct for any remaining unwanted effects in

downstream clustering and differential expression analyses. For each sample, principal component (PC) analysis was performed on a set of highly variable genes defined by Seurat's *FindVariableGenes* function. Genes associated with the resulting PCs (chosen by visual inspection of scree plots, 40 PCs for the human ovarian sample, 45 PCs for the untreated mouse CT26 sample, and 55 PCs for the combined post-treatment CT26 sample) were then used for graph-based cluster identification and subsequent dimensionality reduction using uniform manifold approximation and projection (tSNE). Cluster-based marker identification and differential expression were performed using Seurat's *FindAllMarkers* for all between-cluster comparisons. For analysis of post-treatment mouse CT26 samples, samples were first 93 combined in Seurat using the *MergeSeurat* function, and then the analysis pipeline described above was performed on the aggregated sample in order to ensure that cell identification and clustering was consistent across treatment conditions. Samples objects were then updated to Seurat 3.01 using the *UpdateSeuratObject* to take advantage of enhanced visualization techniques associated with the newer package. Graphs were plotted using built-in functions in Seurat (*tSNEPlot*, *FeaturePlot*, *VlnPlot*, *DotPlot*). For gene set enrichment analysis (GSEA) between treatment conditions, gene lists ranked by average log fold change were generated using *FindAllMarkers* between the indicated treatment conditions using min.pct = 0, and logfc.threshold = 0. These ranked gene lists were analyzed using the fgsea (v1.10.1) package in R.

The correlational analysis between human CD4+/CD8+ T and associated macrophage and monocyte subclusters was carried out by subsetting CD3E/CD3D+ clusters (pan T cell) and CD14+ (pan-macrophage/monocyte) from each of 10 human tumors, processed as described above. Myeloid and T cell objects derived from each patient were updated to Seurat 3.01, and independently normalized using Seurat's *NormalizeData* function (method = LogNormalize and scale.factor = 10000). For each cell type (T and myeloid), per-patient objects were combined using parallelized versions of the functions *FindIntegrationAnchors* and *IntegrateData* using the top 2000 most variable genes per tumor (derived from the *FindVariableGenes* function) and top 30 canonical variates, respectively, in accordance with default parameters suggested by the Seurat website. Initial dimensionality reduction and Louvain clustering were carried out for each of the aggregated T cell and myeloid objects; Tregs, cDC2s, and newly-identified T cell/macrophage doublets were removed and the objects were reclustered using the top 20 PCs. Two tumor-by-cluster matrices were constructed from the 10 aggregated samples, one containing the number of myeloid cells derived from each specific tumor possessing membership within each myeloid subcluster, the other containing similar numbers for each T cell subset. Pearson correlations were generated by comparing the number of cells derived from each myeloid subset to all T cell subsets across the 10 tumors in a pairwise fashion, finally producing the heatmap in Figure 2B. Due to variations in the power to reject normality when comparing myeloid and T cell subsets, we developed a Monte Carlo permutation test to assess statistical significance associated with any observed Pearson's *r*. Null distributions for Pearson's *r* for each comparison were empirically generated by permuting one vector in each comparison 10,000 times. P values were computed by counting the proportion of permuted datasets that yielded an *r* greater than that of the observed data. We provide normalized data matrices for the subset of T and macrophage/monocyte used in this analysis in *Supplemental information*.

For the untreated mouse CT26 and human ovarian samples, the monocyte and TAM clusters were sub-clustered and analyzed using Monocle (v2.12.0) to build single cell trajectories and determine gene expression across pseudotime.

### Tumor and normal tissue TREM2 expression profiling

TREM2 RNA expression plots depicting tumor versus normal tissue differential as well as TREM2 / T cell exhaustion signature correlations were downloaded from the GEPIA2 website ([gepia2.cancer-pku.cn](http://gepia2.cancer-pku.cn)). The GEPIA2 tool is designed for the analysis of RNA

sequencing expression data of 9,736 tumors and 8,587 normal samples from the TCGA and the GTEx projects, using a standard processing pipeline and is developed in the Zhang Lab at Peking University ([Tang et al., 2019](#)).

### Mouse tumor dissociation and flow cytometry staining

Mouse tumor tissue was harvested and placed in ice cold RPMI-1640 (Invitrogen) media. Tumors were enzymatically dissociated using the Mouse Tumor Dissociation Kit (Miltenyi) according to the manufacturer's recommendation. Following dissociation, single cell suspensions were pelleted and tumor supernatant was collected, spun at high speed to remove insoluble material, enzymatically inactivated using Halt Protease Inhibitor Cocktail (Thermo Scientific) and promptly frozen at  $-80^{\circ}\text{C}$  until downstream analysis was performed. Cell pellets were resuspended in stain media (DPBS/1% BSA/2 mM EDTA) and passed through a 100  $\mu\text{m}$  filter to remove undissociated material. Single cell suspensions were counted on a ViCell XR (Beckman Coulter) and plated in 96-well V bottom plates for flow cytometric staining.

Cells were incubated with Zombie NIR (BioLegend), followed by Fc $\gamma$ R block using a combination cocktail of TruStain FcX PLUS (Biolegend), Mouse Serum, Rat Serum, Hamster Serum (Jackson Immuno Research), all prepared in Fc Receptor Blocker (Innovex). Cell surface proteins were stained for 30 minutes on ice, followed by either a secondary stain step or fixation with 1% PFA overnight at  $4^{\circ}\text{C}$ . For staining intracellular proteins, cells were fixed and permeabilized with the FoxP3/Transcription Factor Staining Buffer Set (Thermo Fisher Scientific). Intracellular antibodies were prepared in permeabilization buffer with 2% rat serum and cells were incubated for at least 30 minutes at room temperature. Cells were run on an Attune NXT (ThermoFisher). Flow cytometric analysis was performed using FlowJo (Beckton Dickinson)

### T cell restimulation

Single-cell suspensions from dissociated tumors were cultured in complete RPMI-1640 media with 50 ng/ml PMA (Sigma-Aldrich), 500 ng/ml ionomycin (Thermo Fisher Scientific), and 1X Protein Transport Inhibitor (BD Biosciences) for 5-6 hours at  $37^{\circ}\text{C}$ , 5% CO<sub>2</sub>. Following incubation, stimulated cells were then antibody stained for surface and intracellular proteins as described above.

### Human tumor and flow cytometry staining

Human dissociated tumor cells from Discovery Life Science were thawed in a  $37^{\circ}\text{C}$  water bath and freezing buffer was diluted by slowly adding  $37^{\circ}\text{C}$  media (RPMI with 10% FBS). Cells were pelleted at 400G, washed once with cold PBS, and counted on a ViCell XR (Beckman Coulter).

Cells were incubated with Live/Dead Fixable Aqua (Invitrogen), followed by Fc $\gamma$ R block using a combination cocktail of Human TruStain FcX and True-Stain Monocyte Blocker (Biolegend), Mouse Serum, Rat Serum, Hamster Serum, and Human Serum (Jackson Immuno Research), all prepared in Fc Receptor Blocker (Innovex). Cell surface proteins were stained for 20 minutes on ice. For staining of intracellular proteins, cells were fixed and permeabilized with the FoxP3/Transcription Factor Staining Buffer Set (Thermo Fisher Scientific) per the manufacturer's instructions. Intracellular blocking was done for 20 minutes using a cocktail of Human TruStain FcX and Tru-Stain Monocyte Blocker (Biolegend), Mouse Serum, Rat Serum, Hamster Serum, and Human Serum (Jackson Immuno Research), all prepared in permeabilization buffer. Intracellular antibodies were prepared in permeabilization buffer, added to cells in blocking buffer, and incubated for 20 minutes at room temperature. Cells were washed in stain media and run on a BD FACSAriaFusion (Beckton Dickinson). Flow cytometric analysis was performed using FlowJo (Beckton Dickinson)

### Antibody generation

Anti-TREM2 mAb development was performed as previously described in the WIPO patent application WO2020123664A1. Anti-TREM2 antibodies (fucosylated Anti-TREM2-WT mAb and afucosylated anti-TREM2 mAb) were expressed recombinantly with in Expi293F cells and Expi293F FUT8 knock out cells (kindly provided by University of Toronto). The gene fragments encoding the heavy and light chain residues were codon-optimized for human cell expression. The antibodies were purified from supernatant by Mab-Select PrismA column (GE Healthcare cat# 17549854) using standard protocol. After purification, the antibodies were concentrated and exchanged into PBS.

### Mouse Fc $\gamma$ RIV (ADCC) reporter assay

To perform the Fc $\gamma$ RIV reporter assay we used the Mouse Fc $\gamma$ RIV ADCC Bioassay (Promega). HEK293T cells transduced with murine TREM2 or murine DAP12 were used as targets and the provided Jurkat/Fc $\gamma$ RIV/NFAT-Luc cells provided with the kit were used as effector cells. 25,000 target cells resuspended in RPMI + 10% Fetal Bovine Serum and  $\beta$ -mercaptoethanol were added to white wall 96-well plates (Corning, 25  $\mu\text{l}$ /well). Anti-TREM2 or isotype mAb was prepared in RPMI + 10% Fetal Bovine Serum and  $\beta$ -mercaptoethanol and added to plates containing target cells followed by incubation for 30 minutes at  $37^{\circ}\text{C}$ . Single-use vials of Jurkat/Fc $\gamma$ RIV/NFAT-Luc cells were resuspended in RPMI+10% Fetal Bovine Serum and  $\beta$ -mercaptoethanol and were seeded into white wall 96-well plate (25  $\mu\text{l}$ /well, the effector: target ratio was 3:1), containing the pre-incubated target cell: antibody mixture (50  $\mu\text{l}$ /well), followed by incubation at  $37^{\circ}\text{C}$  for 5 hours. Luciferase activity was measured by using a ONE-Glo Luciferase Assay Reagent (Promega) and Tecan Spark plate reader (Tecan). The luciferase activity was normalized to the negative control, and the percentage of activity was plotted against the concentration of anti-TREM2 mAbs. The EC<sub>50</sub> value of each mAb was calculated by 4-parameter non-linear regression.

**Mouse antibody-dependent cellular phagocytosis (ADCP) assay**

Bone marrow derived macrophages (BMDM) were generated by culturing mouse bone marrow with 25 ng/ml murine CSF-1 in Iscove's Modified Dulbecco's Medium (IMDM), 10% FCS (Hyclone), and Antibiotic-Antimycotic (GIBCO). On day 3 of culture, additional CSF-1 was added to allow for continued BMDM development. On day 6 of culture, 25ng/ml of murine IFN- $\gamma$  (Peprotech) was added to the BMDM culture to induce effector "M1-like" BMDM differentiation. The following day, 100ng/ml LPS (Invivogen) was added to culture 2 hours before use in ADCP assay.

For the ADCP assay, IFN- $\gamma$ /LPS-induced BMDM served as effector cells and GFP+ HEK293T cells transduced with murine TREM2 or murine DAP12 were targets. After harvest, effector BMDM were stained with Cell-Trace Violet dye (Invitrogen) for 20 minutes at 37°C. 50,000 target cells were plated in 96-well U-bottom plates and co-incubated with anti-TREM2 or isotype mAb serially diluted prepared in media for 30 minutes at 37°C. Effector cells were then added to Antibody-Target plates at a 3:1 ratio (150,000 effectors to 50,000 targets) and incubated overnight (18 hours) at 37°C. Following incubation, cells were viability stained using Zombie NIR (Bio-Legend) then fixed using 2% Paraformaldehyde (Invitrogen) for 20 minutes at room temperature prior to being run on an Attune NXT flow cytometer (ThermoFisher). ADCP activity was measured using bead-calculated absolute counts of Cell Trace Violet-, GFP+ cells.

**Cytokine analysis**

Mouse tumor supernatant samples were evaluated for cytokine levels using the V-PLEX mouse cytokine 19-plex kit from Meso Scale Discovery (MSD, Cat. No. K15255D). This product contained two multiplex panels: proinflammatory panel (10 analytes) and cytokine panel (9 analytes). The MSD multiplex assay plates were precoated with capture antibodies. Samples for analysis or kit standards were added at a volume of 50  $\mu$ l per well after pre-diluting the original sample with assay diluent. The plates were washed after a two-hour incubation at room temperature with agitations. Sulfo-tagged detection antibodies were added and incubated for another two hours at room temperature with agitations. Following the incubation, plates were washed once again. 2X Read Substrate was added and plates were read on MSD reader. All data were analyzed by MSD Discovery Workbench® Software 4.0.

**FFPE tissue acquisition**

The ovarian, liver, and colon cancer microarrays (TMA) was purchased from Reveal Biosciences (San Diego, CA) and included patient cases in duplicate cores (2mm<sup>2</sup>) with different diagnoses (Pathology, Grade, and TNM stage). The TMA at Reveal Biosciences was made by acquiring tissues that were fixed in 10% neutral buffer formalin for 24 hours and processed using identical SOPs. Sections were picked onto Superfrost Plus or Startfrost Adhesive slides and all TMAs were cut fresh in 4um serial sections upon ordering and stored at 4°C prior to IHC staining.

**CD8 $\alpha$  IHC staining**

Histology was performed by HistoWiz Inc. based on their institutional SOP and fully automated workflow. All tumor samples (n = 5-6 from each of the 4 treatment groups) were processed, embedded in paraffin, and cut into 4  $\mu$ m thin sections. Immunohistochemistry was performed using a Bond Rx autostainer (Leica Biosystems) with Heat-Induced Epitope Retrieval (HIER) at pH 9.0 for 20 minutes. Antibodies used were biotin conjugated rat anti-mouse monoclonal CD8 $\alpha$  primary antibody (clone 4SM15; eBioscience diluted for use at 1:100 or 5 $\mu$ g/ml) and the Ready-To-Use Novocastra Streptavidin-HRP Detection System by Leica. Bond Polymer Refine Detection (Leica Biosystems) was used according to manufacturer's protocol. After staining, sections were dehydrated and covered using a TissueTek-Prisma and Coverslipper (Sakura). Each slide was scanned at 40x magnification using the Aperio AT2 scanner. Approximately 6 areas delineating the whole tumor were captured at 10x and quantified using ImageJ software (<https://imagej.nih.gov>).

ImageJ was used to quantify the total count of CD8 $\alpha$  expressing cells in each section and expressed as percentage threshold area (percent of pixel in each image) of the section. All images were taken as snapshots under identical conditions such as scales, magnification and similar region of interest. Images were processed by RGB image splitting and blue channel was selected to obtain maximum separation of CD8 $\alpha$  signals from the background tissue. Threshold setting was set between 0 and 110 for all tumors and macro format was used to automate for the batch analysis. Pixel size was selected according to the tissue morphology to exclude false positive staining. Pixel size was selected according to tissue morphology in order to exclude false positive staining. Circularity setting was between 0 and 1 for this quantification in order to capture both non-circular and circular signals in the analysis. The percentage of area and total number of CD8 $\alpha$  counts were measured by ImageJ. For analysis, the cell count average of all images was plotted as mean  $\pm$  the SD to look at CD8 $\alpha$  expression in the tumors of 6 animals (within the mean tumor weight) within each treated group. Dunnett's Multiple Comparisons test was used as the statistical method, with the Isotype serving as the control group comparator. The difference between groups was considered statistically significant when p values were equal or less than 0.05.

**TREM2 IHC staining**

The IHC assay to detect TREM2 positive cells in formalin fixed paraffin embedded (FFPE) tissues was performed according to the steps described here. Slides were first baked in a 60°C oven for 45 minutes followed by deparaffinization three times in xylenes for 5 minutes each. Slides were then rehydrated in a series of ethanol gradient, from 100% to 70% ethanol, and washed at the end with distilled water. The declocker pressure cooker (Biocare) was used for the heat-induced antigen retrieval step in sodium

citrate buffer at pH 6.0 (Sigma, C9999), for 15 minutes at 110°C. To block endogenous peroxidase activity, a blocker solution (Vector Labs) was applied on the slides for 15 minutes followed by rinsing in PBS-T buffer (Alfa Aesar-J63596). Non-specific binding was blocked by incubating the tissue sections with a blocking solution containing goat serum (Vector Labs) overnight at 4°C. PIT2D, also known as the recombinant anti-TREM2 antibody clone EPR20243 (Abcam, ab209814) was used as the primary antibody for 60 minutes at Room Temperature, at a concentration of 5ug/ml in PBS. Slides were then washed twice in PBS-T for 5 minutes each, followed by a 20 minutes incubation in HRP-polymer conjugated anti-rabbit secondary antibody at 1:500 dilution (MP-7500 detection kit from Vector Labs). Slides were washed twice with PBS-T for 5 minutes each before proceeding to the detection step. The DAB substrate was prepared according to the manufacturer's instructions (Abcam, ab64238) and applied to the slides for 3 minutes, followed by rinsing thoroughly in distilled water. Hematoxylin was used to counterstain the slides for 30 s followed by rinsing in running water, dehydration in series of ethanol gradient from 70% to 100% ethanol, and drying in xylenes. The stained slides were finally mounted in media and topped with coverslips for overnight drying.

### Imaging and scoring

After whole slide scanning at 40x using the Aperio AT2 Scanner, quantification and intensity of the TREM2+ cells were assessed by a board-certified pathologist using the following scoring system: **0**: no staining in the stromal area within the core, **1**: ~25% of positive cells in the stromal area within the core, **2**: 50% of positive cells in the stromal area within the core, **3**: 75% of positive cells in the stromal area within the core. Percentages of positive cells that fell between these groups were scored as **0.5** (~12.5%), **1.5** (~37.5%), **2.5** (~62.5%), **and 3.5** (~90%). The intensity of the TREM2 staining was determined as low (score of 1), moderate (score of 2), and strong (score of 3). CD163 staining was used as the positive control to identify the macrophages in the stroma of tumors and normal cores in the serial sections of the TMA (data not shown).

Lost or folded cores with more than half of the area distorted were removed from the analysis and not scored. The H-scores were calculated by using the percentage of cells (0, 12.5, 25, 37.5, 50, 62.5, 75, 90%) with intensity of each markers expression on a four-point semiquantitative scale, this being 0 (null, negative), 1+ (low or weak staining), 2+ (medium or moderate staining), and 3+ (high or strong staining). Thus, scores range from 0 to 300. H-scores were then calculated using the formula:

$$\text{H-Score} = [(\% \text{ at } < 1) \times 0] + [(\% \text{ at } 1+) \times 1] + [(\% \text{ at } 2+) \times 2] + [(\% \text{ at } 3+) \times 3]$$

In the case of TREM2 staining, the intensity was homogeneous in each core and the H-score was therefore calculated by multiplying the frequency of the staining (% positive cells) with the single intensity score.

### QUANTIFICATION AND STATISTICAL ANALYSIS

Unless explicitly stated, data is from a representative experiment of  $\geq 2$  independent experiments. Experimental group assignment was determined through randomization. Unless otherwise noted, error bars represent  $\pm$  SEM calculated using Prism. Apart from bio-informatic work, all Statistical analyses were performed using GraphPad Prism software. Unless noted otherwise, unpaired t tests were used for pairwise comparisons. For statistical measures between more than two groups, one-way ANOVA with multiple comparisons against a control group would be performed unless otherwise noted. Comparisons that did not reach statistical significance are not shown. Investigators were not blinded to group assignment during experimental procedures or analysis.

### ADDITIONAL RESOURCES

A clinical trial sponsored by Pionyr Immunotherapeutics studying the use of anti-human TREM2 (PY314) as a treatment for patients with advanced solid tumors is ongoing. The clinical trial number is NCT04691375 (<https://clinicaltrials.gov/ct2/show/NCT04691375>).